LITHOS 498–499 (2025) 107981

Contents lists available at ScienceDirect

LITHOS

journal homepage: www.elsevier.com/locate/lithos

Filling the gap in the UH*P* metamorphic record of the Liguro-Piemont Lower unit: Insights on fluid-mediated formation of atoll garnets

A. Maffeis [a,*], A. Petroccia [b], S. Nerone [c], F. Caso [d], A. Corno [c], M. Bonazzi [e,f], F. Boero [c], S. Corvò [e,f], S. Ghignone [c], C. Groppo [c,g]

[a] *Dipartimento di Scienze dell'Ambiente e della Terra, Università degli Studi di Milano – Bicocca, Piazza della Scienza 4, 20126 Milano, Italy*
[b] *Dipartimento di Scienze Biologiche, Geologiche ed Ambientali – BiGeA Alma Mater Studiorum, Università di Bologna, Via Zamboni 67, 40126, Italy*
[c] *Dipartimento di Scienze della Terra, Università degli Studi di Torino, Via Valperga Caluso 35, 10125 Torino, Italy*
[d] *Dipartimento di Scienze della Terra "A. Desio", Università degli Studi di Milano, Via Luigi Mangiagalli 34, 20133 Milano, Italy*
[e] *Dipartimento di Scienze della Terra e dell'Ambiente, Università degli Studi di Pavia, Via Ferrata 9, 27100 Pavia, Italy*
[f] *Istituto di Geoscienze e Georisorse di Pavia, IGG-CNR, Via Ferrata 9, 27100 Pavia, Italy*
[g] *Istituto di Geoscienze e Georisorse di Torino, IGG-CNR, Via Valperga Caluso 35, 10125 Torino, Italy*

ARTICLE INFO

Keywords:
Subduction geodynamics
Western Alps
UH*P* eclogite
Coesite
Fluid-rock interaction

ABSTRACT

This contribution investigates the petrologic evolution of a coesite-glaucophane-bearing eclogite belonging to the Liguro-Piemont Lower unit of the Western Alps and explores the formation mechanisms of atoll garnets by integrating petrographic, mineral-chemical, and thermodynamic analyses. The studied eclogite underwent a complex metamorphic history associated with five distinct metamorphic stages: an early greenschist facies stage (<400 °C, <0.6 GPa), two prograde high-pressure stages (early pre-Dp: 450–480 °C, 1.9–2.6 GPa; late pre-Dp: 420–510 °C, 2.3–2.9 GPa), a peak-pressure stage (syn-Dp: 480–580 °C, 2.8–2.9 GPa), and an exhumation stage (post-Dp: 600–630 °C, 1.3–1.5 GPa). The coesite finding links the UH*P* localities already known northward (Cignana) and southward (Monviso and Val di Susa) in the Liguro-Piemont Lower unit, corroborating the coherence of metamorphic evolution across the Western Alps and filling the gap in the UH*P* (Ultra-High Pressure) metamorphic record of this sector of the Liguro-Piemont Lower unit. Mineral inclusion patterns and microstructural features support the involvement of aqueous fluids during atoll garnet formation. Electrolytic fluid modelling suggests a dilute aqueous fluid characterized by dissolved Si and Na, capable of selectively dissolving garnet cores and precipitating secondary garnet and omphacite. The garnet fracturing and exposure of its core is attributed to increasing fluid pressure induced by volume changes (up to 40 % increase of the inclusions' volume) related to the breakdown of the lawsonite included in the garnet mantle and to the associated dehydration reactions. These findings contribute to our understanding of fluid-mediated processes during rock exhumation and highlight the role of aqueous fluids in metamorphic reactions and mineral replacement. Also, our results call for further research to explore the link between atoll garnet formation, fluid-rock interactions, and deep paleoseismicity.

1. Introduction

Exhumed fragments of once subducted oceanic lithosphere provide a window into the physical and chemical processes operating during subduction at depths beyond direct observation (see Brown, 2023 and references therein). Since direct access through deep drilling of currently active subduction zones is limited to the few first kilometres, the petrologic investigation of fossil fragments of oceanic lithosphere in orogenic belts can provide critical geodynamic constraints on subduction architectures and exhumation processes during different stages of the tectonic cycle (see Brown, 2023 and references therein). An accurate understanding of the pressure-temperature (*P*–*T*) evolution of a downgoing slab is also the cornerstone for any study aiming at investigating chemical and petrologic processes occurring within a subducting plate (e.g., Angiboust and Raimondo, 2022). Such knowledge can ultimately also help the experimental and theoretical communities to develop reliable models and simulations of subduction (e.g., van Keken and Wilson, 2023). Moreover, an accurate estimate of the *P*–*T*–*X*

* Corresponding author.
E-mail address: andrea.maffeis@unimib.it (A. Maffeis).

https://doi.org/10.1016/j.lithos.2025.107981
Received 13 July 2024; Received in revised form 18 January 2025; Accepted 29 January 2025
Available online 6 February 2025

conditions allows us to unveil petrological, geochemical and rheological processes (e.g., Frezzotti et al., 2011; Maffeis et al., 2024; Nerone et al., 2024). This especially applies to studies dealing with the production and evolution of subduction zone fluids and those related to ore-forming elements of industrial and economic interest (e.g., C, S, Rare Earth Elements, Transition metals).

Understanding the link between microfabrics development and metamorphic assemblages in deformed metamorphic rocks is crucial for correlating successive deformation episodes with *P*–*T* conditions and determining their relative timing. In addition, for minerals stable over a wide range of *P*–*T* conditions, a detailed investigation of their textures and chemical zoning can provide valuable insights into metamorphic processes. Among several metamorphic minerals stable at high-pressure (H*P*) conditions, garnet records *P*–*T* changes during its growth through the preservation of chemical zoning of both major and trace elements (see Kulhánek and Faryad, 2023 and references therein). Since each compositional domain within garnet reflects a condition of thermodynamic equilibrium with other rock-forming minerals at different stages of the metamorphic and deformation history, garnet is exceptionally useful for estimating the *P*–*T* evolution of metamorphic rocks. However, any compositional modification of the zoning profile occurring after (or during) garnet growth can lead to significant errors in the *P*–*T* estimate. Modification of the zoning profile can be due to several processes; among these, resorption and recrystallization of garnet due to the infiltration of internally or externally derived fluids can lead to element exchange between the dissolving garnet and the matrix and to the simultaneous growth of a new garnet generation (e.g., Bovay et al., 2021; Faryad et al., 2010; Giuntoli et al., 2018; Manzotti et al., 2024). The formation of atoll-shaped garnet is a possible result of such processes (see Hartmeier et al., 2024; Kulhánek et al., 2021 and references therein).

In the Western Alps, remnants of the subducted Liguro-Piemont oceanic lithosphere (L-P; or Piemonte-Liguria domain) are exposed along a 200 km-long and up to 50 km-wide nappe stack (see Agard, 2021; Agard and Handy, 2021). This sector of the Alpine chain is one of the most iconic and best-preserved examples of a fossil subduction zone, providing access to processes that acted from ~30 to ~90 km in depth (see Agard, 2021 and references therein).

Recently, the overall L-P structure has been re-evaluated through a compilation of metamorphic, structural, and lithostratigraphic data by Herviou et al. (2022). They re-defined three distinct units characterized by an almost continuous eastward increase in peak burial conditions from the Liguro-Piemont Upper (LPU) to the Middle (LPM) and Lower (LPL) units (Fig. 1a). These units followed a prograde cold metamorphic

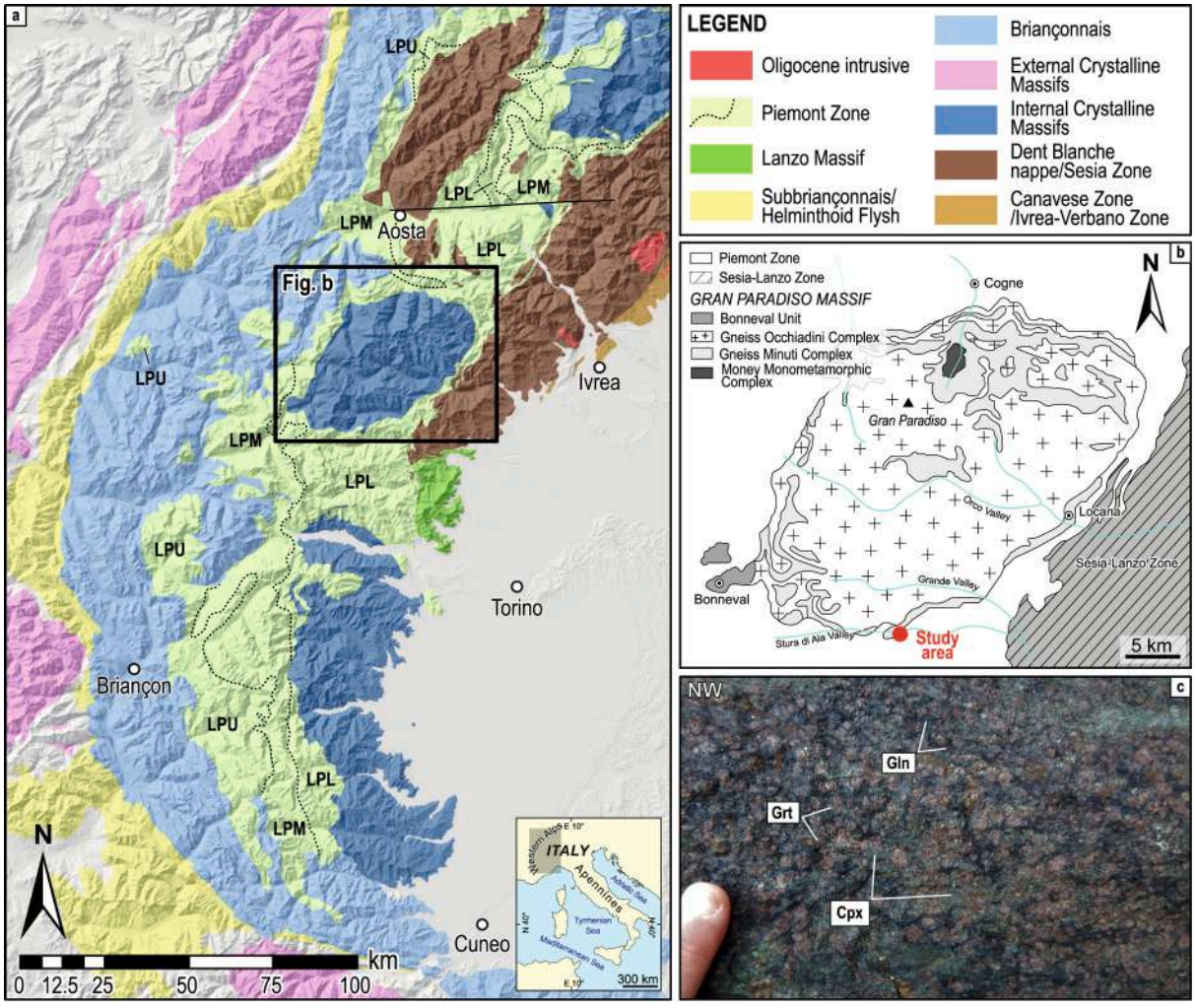

Fig. 1. a) Geological sketch map of the Western Alps with the distinction of the Liguro-Piemont Upper units (LPU; average peak at ~370 °C, 1.7 GPa), Middle units (LPM; average peak at ~470 °C, 2.0 GPa) and Lower units (LPL; average peak at ~550 °C, 2.5 GPa), modified after Bigi et al. (1990). The black line close to Aosta displays the Aosta-Ranzola fault. b) Simplified geological map of the Gran Paradiso Massif with the location of the study area, modified after Gasco and Gattiglio (2011). For a more detailed map see Caso et al. (2021). c) Mesoscale view of the coesite-glaucophane-bearing eclogite: note the typical eclogite assemblage, made by garnet (red), clinopyroxene (green) and Na-amphibole (blue). (For interpretation of the references to colour in this figure legend, the reader is referred to the web version of this article.)

gradient of ~7–8 °C/km (assuming, for simplicity, *P* as lithostatic; Agard, 2021). Despite their extensive and detailed compilation of *P–T* conditions, Herviou et al. (2022) highlighted the lack of data in certain areas, as well as the lack of statistically significant geographic coverage, especially in the LPL. One of these gaps concerns the LPL rocks exposed close to the contact with the southern Gran Paradiso Massif. Also, the recent discovery of ultra-high pressure (UH*P*) evidence from the LPL (Ghignone et al., 2023, 2024) raises questions on the homogeneity of the subduction *T/P* gradient and of the metamorphic peak experienced by the oceanic domains of the Western Alps.

This study aims to fill such a gap by investigating an exceptionally preserved eclogitic coesite-glaucophane-bearing Fe-Ti metagabbro sampled in the LPL at the southern contact with the Gran Paradiso Massif (Fig. 1b, c). Furthermore, thanks to the peculiar characteristics of the studied rock, the role of H*P*/UH*P* subduction-zone fluids in developing atoll garnet is also explored.

2. Geological setting

The Western Alps are the result of the east- to south-east-dipping, slow (~1 cm/yr) subduction of the Valais and Ligurian-Piemont oceans, interposed between the Adriatic and European continental margins (e.g., Agard and Handy, 2021). In their axial sector, the Western Alps consist of continental- and oceanic-derived rocks which reached H*P*/UH*P* conditions during the Alpine subduction; remnants of subducted L-P oceanic lithosphere are now exposed structurally above the eclogite-facies continental-derived Internal Crystalline Massifs (Fig. 1a; i.e., Dora Maira, Gran Paradiso, Monte Rosa). Historically, the L-P domain has been subdivided based on its lithostratigraphic features and metamorphic evolution (Bearth, 1967). The lowermost units, directly overlying the Internal Crystalline Massifs, are ascribed to the Zermatt-Saas-like units or Lower/Internal Piemont Zone (LPZ/IPZ) and are made of remnants of oceanic lithosphere with a minor metasedimentary cover. On the other hand, the uppermost units are ascribed to the Combin-like units (Bearth, 1967) or Upper/External Piemont Zone (UPZ/EPZ) and are made mainly of metasedimentary rocks with scattered lenses of oceanic lithosphere.

The LPZ/IPZ units experienced eclogite-facies peak Alpine metamorphism, with local UH*P* conditions (Frezzotti et al., 2011; Ghignone et al., 2023, 2024; Reinecke, 1998), while UPZ/EPZ units registered blueschist- to greenschist-facies metamorphic peak (e.g., Corno et al., 2023; see Herviou et al., 2022 for a review). Recently, this traditional subdivision of the L-P domain has been revised by Herviou et al. (2022), who proposed a trimodal distribution of units with an almost continuous increase in metamorphic conditions from the Upper units (LPU; average peak at ~370 °C, 1.7 GPa) to the Middle units (LPM; average peak at ~470 °C, 2.0 GPa) and to the Lower units (LPL; average peak at ~550 °C, 2.5 GPa). The LPU and LPM units, metamorphosed under blueschist-facies conditions, are dominated by sediments (>90 %) and can thus be correlated with the UPZ/EPZ units. The LPL units, metamorphosed at eclogite-facies conditions, are instead much richer in mafic-ultramafic rocks (>40 %). This work follows the L-P subdivision and nomenclature of Herviou et al. (2022; see Fig. 1a).

The studied samples have been collected from the LPL of the middle Ala Valley in the NW of Italy. This area has been historically investigated for the exploitation of iron ore deposits in ultramafic-hosted magnetite mineralization (Galliano et al., 2022 and references therein). A thorough study of the lithostratigraphic and petrographic features of the LPL in the Ala Valley was conducted by Leardi and Rossetti (1985) and references therein, reporting the occurrence of a complete metamorphosed oceanic sequence, from the serpentinised mantle to the metasedimentary cover. Minimum *P–T* peak conditions of 1.3 GPa and 450–460 °C and retrograde *P* conditions of 0.8 ± 0.3 GPa were constrained for this sequence (Sandrone et al., 1986). Notably, such a blueschist- to epidote-amphibolite-facies evolution is not in agreement with the metamorphic gradient of the belt. Nevertheless, this area comprises large portions of completely retrogressed meta-ophiolitic rocks, interleaved with minor, well-preserved eclogitic rocks, providing promising clues for refining the metamorphic conditions of this area (De Togni et al., 2024; Sandrone et al., 1986). A renewed interest in the area prompted fieldwork aimed at constraining the litho-structural setting (Assanelli and Roda, 2023; Caso et al., 2021) and the timing of magmatic accretion in the Ala Valley (De Togni et al., 2024), as well as the litho-structural setting of the neighbouring Stura di Viù Valley (De Togni et al., 2021).

The coesite-glaucophane-bearing eclogitic rock investigated in this study comes from an LPL Fe-Ti meta-gabbro body embedded within metabasite exposed above the village of Martassina, close to the contact with the structurally lower Gran Paradiso Massif (Caso et al., 2021; Leardi and Rossetti, 1985; Fig. 1b, c).

3. Methods

3.1. Rock and mineral chemistry

3.1.1. SEM-EDS analyses and maps

Petrographic identification of fine-grained minerals was performed by a scanning electron microscope (SEM) JEOL JSM-IT300LV, equipped with an energy-dispersive spectrometer (EDS) Energy 200 System and an SSD X-Act3 detector (Oxford Inca Energy), hosted at the Department of Earth Sciences, University of Turin (Italy). The experimental conditions include the following: accelerating voltage 15 kV, counting time 20 s, process time 1, and a working distance of 10 mm. The energy-dispersive X-ray spectrometer-acquired spectra were corrected and calibrated both in energy and in intensity thanks to measurements performed on cobalt standard introduced in the vacuum chamber with the samples. The Microanalysis Suite Oxford INCA Energy 300, which enables spectra visualisation and elements recognition, was employed. A ZAF data reduction program was used for spectra quantification. The resulting full quantitative analyses were performed (e.g., Bullock et al., 2025), using natural oxides and silicates from Astimex Scientific Limited, as standards. Quantitative mineral chemical analyses were normalized through the software NORM (Ulmer, 1986, updated 2013). Structural formulae have been calculated based on 12 oxygens for garnet, 8 for albite, 6 for omphacite, 23 for amphibole, 11 for white mica, and 12.5 for epidote. After calculating their stoichiometric Fe_2O_3 content by NORM, amphiboles have been classified following IMA guidelines (Hawthorne et al., 2012) as implemented by Locock (2014) in an Excel spreadsheet. A statistical test regarding the reliability of EDS analyses relative to fewer WDS analyses used for chemical map calibration can be found in the Supplementary Material (Supplementary Fig. 1).

X-ray maps of inclusion-bearing sulfides have been acquired using the same SEM-EDS instrument, in order to measure the compositional variability of the studied minerals at the local scale and to investigate the relationships between compositional zoning and microstructures. Operative conditions used for mapping were the following: 15 kV accelerating voltage, 5 nA probe current, 1 µs EDS process time, 2.5 µm point step, and 1 ms dwell time. Representative mineral analyses are provided in Table 2; the complete mineral composition dataset can be found in Supplementary Table 1.

3.1.2. WDS analyses and maps

Electron probe micro-analyses were performed with the JEOL JXA 8200 electron probe micro-analyzer (EPMA) located at the Institute of Geological Sciences of the University of Bern, Switzerland. The EPMA session includes two steps: acquisition of X-ray compositional maps of the whole thin section and measurement of point analyses for map calibration. Spot analyses were acquired using a 1 µm electron beam diameter, 15 keV accelerating voltage and 20 nA specimen current. X-ray intensities were all obtained by WDS with 20 s counting time on peak positions and 10 s counting time on each background position. The

following natural and synthetic standards were used for the calibration: almandine (SiO_2, Al_2O_3, and FeO), anorthite (CaO), orthoclase (K_2O), albite (Na_2O), forsterite (MgO), rutile (TiO_2) and pyrolusite (MnO).

Analytical conditions were: 15 kV accelerating voltage, 100 nA specimen current, 60 ms dwell time, and a step size (corresponding to the pixel size in the final images) of 20 μm. Nine elements (Si, Ti, Al, Fe, Mn, Mg, Na, Ca, and K) were measured at the specific wavelength in two passes using five wavelength-dispersive spectrometers (WDS).

The JEOL JXA-8200 Superprobe EPMA hosted at the Department of Earth Sciences "A. Desio", University of Milan (Italy) was used to acquire X-ray maps on selected garnet porphyroblasts. The operative conditions of WDS maps of Mg, Si, Ca, Mn and Fe were: 15 kV accelerating voltage, 100 nA probe current, 6 μm step size, and 45 ms dwell time.

3.1.3. Bulk rock composition

The software XMapTools v4.1 (Lanari et al., 2014) was used for the processing of the whole thin section map, including (i) classification, (ii) production of mineral distribution maps, (iii) identification of compositional variation within these minerals and (iv) calculation of mineral modes. Quantitative point analyses within the map area were used to calibrate X-ray maps. Given the observed mineral zoning, the effective (local) bulk rock composition was obtained through a mass-balance calculation which combines mineral modes with the average mineral compositions. The following strategy was applied: (i) the thin magnetite rim developed around pyrite due to atmospheric oxidation was converted into pyrite; (ii) albite and titanite filling the narrow late veins cutting through the sample were excluded; (iii) apatite was excluded, and (iv) the different growth stages of garnet, classified and quantified by XMapTools, were fractionated. Therefore, three effective bulk compositions (EBC) for the entire thin section were calculated by fractionating the different garnet domains: EBC I is the entire bulk rock composition without garnet fractionation; EBC II fractionates the core of the garnet, and EBC III accounts for garnet core and mantle fractionation (Table 1). The fractionation process results, for example, in a relative decrease in the amount of MnO and CaO and an increase in MgO in the fractionated EBC II and EBC III. Representative mineral analyses are provided in Table 2; the complete mineral composition dataset used for bulk rock mass balance reconstruction can be found in Supplementary Table 1.

Table 1
Effective bulk rock compositions (EBC) used for phase diagrams computation. EBC I, II and III are used for phase diagrams in Figs. 9-11. EBC I + H_2O is used for electrolytic fluid calculations reported in Fig. 13. The local bulk composition of Grt + Lws pseudomorphs is used for the phase diagram in Fig. 14. Elemental rather than element oxide components are generally preferred for electrolytic fluid phase diagram calculations; however, element oxides have been used in this case to simplify calculations, given the semi-qualitative nature of the calculations and the fact that the fluid speciation (which is the point most impacted by the choice of system components) is ignored.

		EBC I	EBC II	EBC III	EBC I + H_2O	Local bulk composition for Grt + Lws pseudomorphs
mol %	SiO_2	48.430	48.628	49.649	48.430	35.516
	TiO_2	3.525	3.253	3.775	3.525	
	Al_2O_3	7.584	7.272	6.200	7.584	13.492
	FeO_{TOT}	21.676	21.786	20.159	21.676	16.543
	MnO	0.532	0.493	0.378	0.532	0.612
	MgO	7.697	7.926	8.729	7.697	1.419
	CaO	4.774	4.599	4.130	4.774	9.606
	Na_2O	4.183	4.377	5.093	4.183	0.978
	H_2O				3.150	21.251
	S_2	0.739	0.773	0.899	0.739	
	O_2	0.859	0.892	0.988	0.859	0.583

3.1.4. Raman spectroscopy

The Raman spectra of coesite inclusions in garnet were measured at the University of Pavia with a Horiba LabRam HR Evolution spectrometer (holographic gratings of 1800 grooves/mm) equipped with an Olympus BX41 confocal microscope. The equipment was operated at controlled temperature of 20 ± 1 °C. Raman spectra were excited using the 532 nm line of a solid-state (YAG) laser. The laser power on the sample surface was approximately 1 to 2 mW and a laser spot of ~2 μm. The spectrometer was calibrated to the Raman peak of silicon at 520.5 cm^{-1}. The collected spectra were baseline-corrected and normalized to the acquisition time. Peak positions, full-width at half maximum (FWHM), and integrated intensities were determined from fits with pseudo-Voigt functions. Each Raman measurement was performed at the inclusion centre. All Raman spectra were acquired with four repetitions of 30 s.

3.1.5. LA-ICP-MS

The trace-element concentrations of rutile were determined by laser ablation inductively coupled plasma mass spectrometry (LA-ICP-MS) at the Istituto di Geoscienze e Georisorse of the National Research Council in Pavia, Italy. The instrument couples an Excimer Laser 193 nm ArF (GeoLas200 Microlas) with a Triple Quadrupole (8900 QQQ from Agilent). The laser was operated at 10 Hz frequency. The signals of the following 31 masses were acquired during the analytical runs: ^{25}Mg, ^{27}Al, ^{29}Si, ^{45}Sc, ^{49}Ti, ^{51}V, ^{53}Cr, ^{55}Mn, ^{57}Fe, ^{59}Co, ^{60}Ni, ^{63}Cu, ^{66}Zn, ^{85}Rb, ^{88}Sr, ^{89}Y, ^{90}Zr, ^{93}Nb, ^{95}Mo, ^{98}Mo, ^{118}Sn, ^{121}Sb, ^{177}Hf, ^{178}Hf, ^{181}Ta, ^{181}W, ^{182}W, ^{201}Hg, ^{208}Pb, ^{232}Th and ^{238}U. Single sample analysis consisted of 1 min of background acquisition and 1 min of sample ablation. NIST-SRM610 was used as an external standard, whereas Ti was adopted as an internal standard for rutile. In each analytical run, the USGS reference samples BCR2, NIST612, R69, R13 (Rocholl et al., 1997) were analyzed together with the unknowns for quality control. Precision and accuracy are better than 10 %, for all standards analyzed. Data reduction was performed with the Glitter software package (van Actherbergh, 2001). The analyses were performed both on separated rutile grains and in situ using a laser beam of 50 μm in diameter.

3.2. Thermodynamic modelling

Compositional and isochemical phase diagrams were calculated for EBC I, EBC II and EBC III in the 11-component MnNCFMAST-SOH (MnO–Na_2O–CaO–FeO_{tot}–MgO–Al_2O_3–SiO_2–TiO_2–S_2–O_2–H_2O) system using Perple_X 7.1.1 (Connolly, 2009). Due to the contemporaneous presence of pyrite and Fe^{3+}-bearing phases, for modelling purposes, Fe_2O_3 was replaced by O_2 as a system component. Initial O_2 bulk content was derived from the stoichiometrically determined Fe_2O_3 from minerochemical data, and the corresponding Fe was added to FeO_{tot}. Further refinements of bulk O_2 were performed by thermodynamic $T(P)$–O_2 modelling. For the calculations, the internally consistent thermodynamic database for condensed phases of Holland and Powell (2011) (ds622) and the equation of state for the binary fluid H_2O–CO_2 of Holland and Powell (1998) have been adopted. For simplicity, fluid saturation conditions have been assumed with a pure H_2O fluid phase (i.e., $aH_2O = 1$). The following solution models were used: garnet, chloritoid, chlorite, and ilmenite (White et al., 2014), clinopyroxene (Green et al., 2007, modified as specified in Green et al., 2016), amphibole (Green et al., 2016), feldspar (Fuhrman and Lindsley, 1988), ideal talc, the non-ideal margarite-paragonite, pyrrhotite (Evans et al., 2010); an ad hoc pumpellyite model and olivine and orthopyroxene (Holland et al., 2018). Pure mineral phases are silica polymorphs, pyrite, rutile, titanite, lawsonite, and anhydrite.

Electrolytic-fluid thermodynamic modelling, used for estimating the solute-bearing fluid composition at H*P* conditions during atoll garnet formation, was performed with the Lagged-Speciation algorithm

Table 2
Representative mineral compositions from SEM-EDS. The complete dataset can be found in Supplementary Table 1. In amphibole analyses "A", "B" and "C" stand for the crystalline sites occupied by each cation.

#Analysis	425_GRT	426_GRT	1F_GRT_019	464_GRT	448_GRT	1F_GRT_015	479_GRT	476_GRT	1F_GRT_074	029_GRT	1F_GRT_046
Gen.	Grt_{1C}	Grt_{1C}	Grt_{1C}	Grt_{1M}	Grt_{1M}	Grt_{1M}	Grt_{1R}	Grt_{1R}	Grt_{1R}	Grt_{2S}	Grt_{2S}
						wt%					
SiO_2	36.96	37.08	37.90	36.71	37.16	37.64	36.60	36.95	37.13	37.65	37.88
TiO_2	0.20	0.07	0.00	0.12	0.15	0.00	0.05	0.04	0.00	0.06	0.00
Al_2O_3	21.22	20.54	20.95	20.44	20.81	20.73	20.47	20.62	20.55	20.64	21.26
Cr_2O_3	0.00	0.10	0.00	0.03	0.01	0.00	0.02	0.02	0.00	0.00	0.00
Fe_2O_3	0.62	1.13	1.21	1.18	0.79	0.75	1.36	0.88	1.43	0.03	0.18
FeO	31.57	31.16	32.74	32.49	32.75	32.74	33.90	34.63	35.35	33.16	35.17
MnO	1.32	1.70	1.00	0.48	0.40	0.68	0.93	0.74	0.93	3.38	1.92
MgO	2.40	2.09	1.80	2.53	2.13	2.19	3.14	2.85	2.54	2.28	2.83
CaO	5.62	6.08	6.52	5.09	5.94	5.99	2.62	2.93	2.80	3.46	2.44
Total	99.86	99.96	102.13	99.07	100.14	100.73	99.10	99.67	100.72	100.75	101.68
						a.p.f.u.					
Si	2.97	2.98	2.99	2.98	2.98	3.00	2.97	2.99	2.98	3.02	3.00
Ti	0.01	0.00	0.00	0.01	0.01	0.00	0.00	0.00	0.00	0.00	0.00
Al	2.01	1.95	1.95	1.95	1.97	1.95	1.96	1.96	1.95	1.95	1.99
Cr	0.00	0.01	0.00	0.00	0.00	0.00	0.00	0.00	0.00	0.00	0.00
Fe^{3+}	0.04	0.07	0.07	0.07	0.05	0.05	0.08	0.05	0.09	0.00	0.01
Fe^{2+}	2.12	2.10	2.16	2.20	2.20	2.18	2.30	2.34	2.38	2.22	2.33
Mn	0.09	0.12	0.07	0.03	0.03	0.05	0.06	0.05	0.06	0.23	0.13
Mg	0.29	0.25	0.21	0.31	0.25	0.26	0.38	0.34	0.30	0.27	0.33
Ca	0.48	0.52	0.55	0.44	0.51	0.51	0.23	0.25	0.24	0.30	0.21
Grs	0.14	0.14	0.15	0.11	0.14	0.15	0.03	0.06	0.04	0.10	0.06
Alm	0.71	0.70	0.72	0.74	0.74	0.73	0.77	0.78	0.80	0.74	0.78
Prp	0.10	0.08	0.07	0.10	0.09	0.09	0.13	0.12	0.10	0.09	0.11
Sps	0.03	0.04	0.02	0.01	0.01	0.02	0.02	0.02	0.02	0.08	0.04
And	0.02	0.03	0.04	0.04	0.02	0.02	0.04	0.03	0.04	0.00	0.01
Uva	0.00	0.00	0.00	0.00	0.00	0.00	0.00	0.00	0.00	0.00	0.00
Ti-AlGrt	0.01	0.00	0.00	0.00	0.00	0.00	0.00	0.00	0.00	0.00	0.00

#Analysis	223_GLN	227_GLN	1F_GLN_269	175_GLN	312_GLN	507_GLN	508_GLN	304_GLN	510_GLN	318_GLN	1F_AMP_341
Gen	Amp_1	Amp_1	Amp_1	Amp_2	Amp_2	Amp_2	Amp_3	Amp_3	Amp_4	Amp_4	Amp_4
Species	Gln	Gln	Gln	Gln	Fgln	Gln	Fgln	Foktp	Foktp	Wnc	Fwnc
						wt%					
SiO_2	56.39	56.94	57.83	56.30	55.99	56.87	55.30	44.81	54.96	52.39	50.28
TiO_2	0.01	0.00	0.00	0.12	0.03	0.00	0.04	0.48	0.00	0.12	0.07
Al_2O_3	5.67	5.68	5.40	5.93	6.30	6.67	8.34	12.57	5.29	2.44	5.33
Cr_2O_3	0.00	0.00	0.00	0.00	0.00	0.00	0.00	0.00	0.00	0.00	0.00
MnO	0.00	0.00	0.06	0.00	0.00	0.02	0.00	0.07	0.00	0.04	0.11
FeO	10.28	8.67	16.98	12.62	12.53	9.64	15.56	18.37	20.92	13.78	15.42
Fe_2O_3	6.76	7.13	0.00	5.48	6.02	6.21	3.15	3.70	0.00	4.37	5.86
MgO	10.53	11.35	10.60	9.68	8.99	10.82	7.54	6.91	6.67	12.47	10.18
CaO	1.74	1.70	1.01	2.10	1.30	1.12	1.24	6.95	5.52	7.40	6.11
Na_2O	6.24	6.47	6.65	6.26	6.69	6.79	6.86	5.22	5.83	3.27	4.31
K_2O	0.00	0.07	0.04	0.00	0.02	0.00	0.00	0.31	0.00	0.00	0.00
H_2O^+	2.12	2.13	2.12	2.12	2.11	2.14	2.10	2.02	2.06	2.03	2.03
F	0.00	0.00	0.00	0.00	0.00	0.00	0.00	0.00	0.00	0.00	0.00
Cl	0.00	0.03	0.02	0.00	0.01	0.04	0.00	0.02	0.02	0.00	0.00
O=F,Cl	0.00	0.00	0.00	0.00	0.00	0.00	0.00	0.00	0.00	0.00	0.00
Initial Tot.	99.74	100.16	98.59	100.61	100.00	100.31	100.13	101.42	101.27	98.31	99.70
Final Tot.	99.74	100.16	100.71	100.61	99.99	100.30	100.13	101.39	101.27	98.34	99.70
						a.p.f.u.					
Si	7.97	7.97	8.17	7.96	7.96	7.95	7.89	6.64	7.99	7.75	7.43
Al $^{(IV)}$	0.03	0.03	0.00	0.04	0.04	0.05	0.11	1.36	0.01	0.25	0.57
Ti $^{(IV)}$	0.00	0.00	0.00	0.00	0.00	0.00	0.00	0.00	0.00	0.00	0.00
$Fe^{3+(IV)}$	0.00	0.00	0.00	0.00	0.00	0.00	0.00	0.00	0.00	0.00	0.00
Ti $^{(VI)}$ C	0.00	0.00	0.00	0.01	0.00	0.00	0.01	0.05	0.00	0.01	0.01
Al $^{(VI)}$ C	0.92	0.91	0.90	0.94	1.02	1.05	1.29	0.84	0.89	0.18	0.36
Cr C	0.00	0.00	0.00	0.00	0.00	0.00	0.00	0.00	0.00	0.00	0.00
Mn^{3+} C	0.00	0.00	0.00	0.00	0.00	0.00	0.00	0.00	0.00	0.00	0.00
Fe^{3+} C	0.72	0.75	0.00	0.58	0.64	0.65	0.34	0.41	0.00	0.49	0.65
Mn^{2+} C	0.00	0.00	0.00	0.00	0.00	0.00	0.00	0.00	0.00	0.00	0.00
Fe^{2+} C	1.14	0.97	1.87	1.42	1.43	1.04	1.76	2.17	2.54	1.57	1.74
Mg C	2.22	2.37	2.23	2.04	1.91	2.26	1.60	1.53	1.45	2.75	2.24
Mn^{2+} B	0.00	0.00	0.01	0.00	0.00	0.00	0.00	0.01	0.00	0.01	0.01
Fe^{2+} B	0.07	0.05	0.14	0.07	0.06	0.08	0.10	0.11	0.00	0.13	0.17
Mg B	0.00	0.00	0.00	0.00	0.00	0.00	0.00	0.00	0.00	0.00	0.00
Ca B	0.26	0.26	0.15	0.32	0.20	0.17	0.19	1.10	0.86	1.17	0.97
Na B	1.66	1.70	1.70	1.61	1.74	1.75	1.71	0.78	1.14	0.69	0.85
Ca A	0.00	0.00	0.00	0.00	0.00	0.00	0.00	0.00	0.00	0.00	0.00
Na A	0.05	0.06	0.12	0.10	0.10	0.09	0.19	0.72	0.50	0.25	0.39

(*continued on next page*)

Table 2 (*continued*)

#Analysis	223_GLN	227_GLN	1F_GLN_269	175_GLN	312_GLN	507_GLN	508_GLN	304_GLN	510_GLN	318_GLN	1F_AMP_341
K A	0.00	0.01	0.01	0.00	0.00	0.00	0.00	0.06	0.00	0.00	0.00
O (non-W)	22.00	22.00	22.00	22.00	22.00	22.00	22.00	22.00	22.00	22.00	22.00
OH	2.00	1.99	2.00	2.00	2.00	2.00	2.00	2.00	2.00	2.00	2.00
F	0.00	0.00	0.00	0.00	0.00	0.00	0.00	0.00	0.00	0.00	0.00
Cl	0.00	0.01	0.01	0.00	0.00	0.01	0.00	0.01	0.00	0.00	0.00
O	0.00	0.00	0.00	0.00	0.00	0.00	0.00	0.00	0.00	0.00	0.00

#Analysis	1F_262	1F_CPX_314	124_OMP	461_OMP	1F_246	468_omp	647_OMP	432_OMP
Gen	Cpx_1	Cpx_1	Cpx_2	Cpx_2	Cpx_3	Cpx_3	Cpx_4	Cpx_4
				wt%				
SiO_2	52.29	52.15	54.67	54.18	54.40	54.67	54.65	55.05
TiO_2	0.00	0.00	0.00	0.12	0.00	0.10	0.08	0.06
Al_2O_3	0.80	0.37	7.47	8.91	5.66	6.84	6.66	9.41
Cr_2O_3	0.03	0.00	0.10	0.07	0.01	0.19	0.01	0.04
Fe_2O_3	18.57	17.90	9.93	9.82	14.44	14.78	14.20	12.65
FeO	9.40	5.61	4.25	3.61	3.22	3.01	3.05	2.64
MnO	0.31	0.00	0.09	0.03	0.09	0.00	0.03	0.00
MgO	3.28	4.90	5.13	4.70	4.78	4.39	4.49	3.58
CaO	7.84	10.95	9.12	8.22	8.51	7.07	7.63	6.08
Na_2O	7.71	7.17	8.38	9.16	9.05	9.89	9.50	10.57
Total	100.24	99.05	99.23	98.82	100.16	100.94	100.31	100.11
				a.p.f.u.				
Si	2.01	2.01	2.01	1.99	2.00	1.99	2.00	2.00
Ti	0.00	0.00	0.00	0.00	0.00	0.00	0.00	0.00
Al	0.04	0.02	0.32	0.39	0.25	0.29	0.29	0.40
Cr	0.00	0.00	0.00	0.00	0.00	0.01	0.00	0.00
Fe^{3+}	0.54	0.52	0.27	0.27	0.40	0.41	0.39	0.35
Fe^{2+}	0.30	0.18	0.13	0.11	0.10	0.09	0.09	0.08
Mn	0.01	0.00	0.00	0.00	0.00	0.00	0.00	0.00
Mg	0.19	0.28	0.28	0.26	0.26	0.24	0.25	0.19
Ca	0.32	0.45	0.36	0.32	0.34	0.28	0.30	0.24
Na	0.58	0.54	0.60	0.65	0.65	0.70	0.67	0.74
Wo	0.16	0.23	0.18	0.16	0.17	0.14	0.15	0.12
En	0.10	0.14	0.14	0.13	0.13	0.12	0.12	0.10
Fs	0.15	0.09	0.07	0.06	0.05	0.05	0.05	0.04
Pxm	0.01	0.00	0.00	0.00	0.00	0.00	0.00	0.00
Acm	0.55	0.52	0.28	0.27	0.40	0.41	0.39	0.35
Jd	0.04	0.02	0.33	0.38	0.25	0.29	0.28	0.40
$CaTiAl_2O_6$	0.00	0.00	0.00	0.00	0.00	0.00	0.00	0.00

implemented in Perple_X (Connolly and Galvez, 2018; Galvez et al., 2015) using the internally consistent thermodynamic database for condensed phases of Holland and Powell (2011) (ds622) and solute species data from the DEW/HKF model of Sverjensky et al., 2014 (revised 2017). The properties of H_2O, H_2, O_2, H_2S, and SO_2 were described using the solvent reference state via the linear Generic Hybrid Fluid model implemented in Perple_X (COH-Fluid; Connolly and Galvez, 2018). Electrolytic fluid calculations do not allow for fluid-saturated conditions to be imposed; therefore, an appropriate amount of initial fluid in the system composition must be fixed. Since atoll garnet formation implies that the originally fractionated garnet core and mantle become available for further reaction with the entire rock system, the unfractionated EBC I with a fixed amount of H_2O was used. The amount of H_2O was fixed at that present in the system at HP (e.g., Manzotti et al., 2020), in correspondence to the last major dehydration reaction encountered along the reconstructed *P–T* path (i.e., the Lws-out reaction).

Post-entrapment modelling of lawsonite inclusions in garnet porphyroblasts was performed using a representative local bulk composition obtained by taking 1 mol of host garnet mantle and one mole of lawsonite pseudomorphs (following the rationale first proposed by Carvalho et al., 2020), now represented by paragonite and zoned epidote. The proportion of paragonite and epidote was retrieved from image analyses of BSE images. To properly reproduce the observed microstructures and phase proportions, and since the lawsonite breakdown releases a substantial amount of fluid, we reintegrated in the local bulk composition the amount of H_2O present in the sub-system garnet+lawsonite at the moment of lawsonite entrapment during garnet growth. This was constrained by performing a preliminary calculation at H_2O saturated conditions and then by selecting the H_2O content at the supposed lawsonite entrapment conditions (~470 °C, 2.4 GPa). The local bulk composition obtained through this approach represents a sub-system that followed its own metamorphic evolution once it was isolated from the rest of the chemical system represented by the whole rock. Isochemical phase diagram calculations were performed in the MnNCFMAS-OH sub-system with a setup identical to the one used for the other isochemical phase diagrams presented above. The changes in modal amounts of each phase were computed relative to their volume proportions at the supposed lawsonite entrapment conditions along the reconstructed *P–T* path (i.e., ~470 °C - 2.4 GPa).

3.3. Sample petrography, microstructures and mineral chemistry

Thin sections were prepared parallel to the XZ plane of the corresponding finite strain ellipsoid (i.e., parallel to the lineation and perpendicular to the main foliation; see Caso et al., 2024 for a discussion about the consequences of modelling using different planes). The description of the structural elements and their orientations follows Caso et al. (2021). To describe the structural architecture of the studied area without bias from the previous investigations, the sequence of deformation events and structural elements are numbered relative to the principal deformation event (e.g., Dp, Dp-1), where the subscript "p" denotes "principal" whereas "D" denotes "deformation". Mineral abbreviations follow Warr (2021).

3.4. Rock overview

The investigated coesite-glaucophane-bearing eclogite sample (GPS coordinates: N45°19′02″–E7°14′39″; Fig. 1c) comes from a Fe-Ti metagabbro boudin (~3 m long and 2 m wide) embedded in glaucophane-rich metabasites (see Figs. 2 and 3 in Caso et al., 2021 for meso- and micro-structures of metabasites).

At the mesoscale, the coesite-glaucophane-bearing eclogite displays a spaced and discontinuous foliation with pluri-millimetre garnet and glaucophane (Fig. 1c). To obtain a reliable petrographic characterization, six thin sections (GP21-1B, GP21-1C, GP21-1D, GP21-1E, GP21-1F, GP21-1G) were obtained from the same hand specimen. Sample GP21-1B and sample GP21-1F have been chosen for in situ minero-chemical analyses since they display a well-preserved mineral assemblage, and microstructures suitable to determine equilibrium *P–T* conditions. The petrography, blastesis–deformation relationships and mineral chemistry characterization of samples GP21-1B and GP21-1F are shown in Figs. 2-7.

Both samples GP21-1B and GP21-1F are coarse-grained and are characterized at the microscale by a banded structure made of

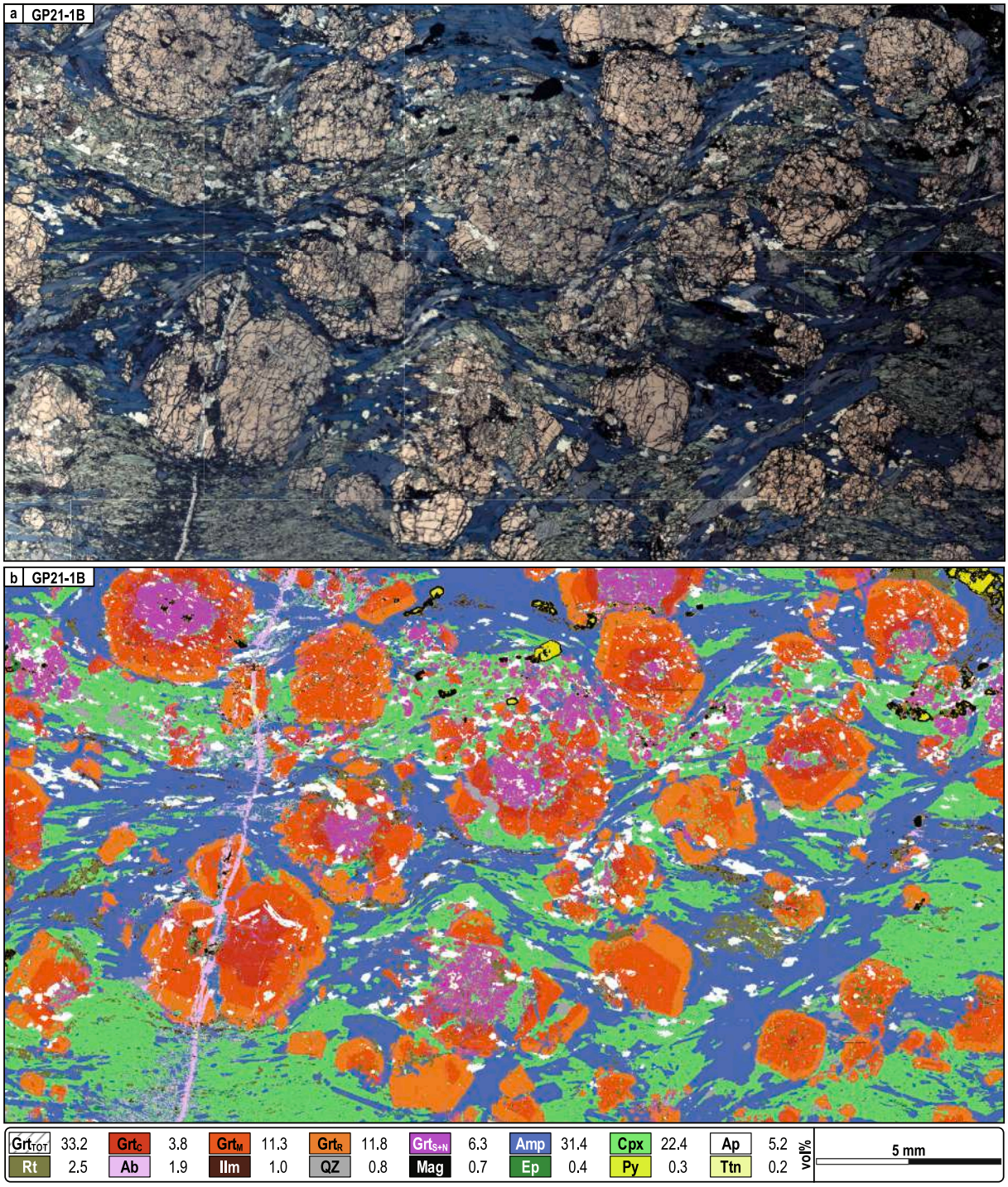

Fig. 2. a) Plane polarised scan (PPL) of sample GP21-1B corresponding to the area mapped through the WDS. b) Mineral modal map of sample GP21-1B resulting from processing the collected chemical maps with XMapTools (Lanari et al., 2014). The modal proportions of the processed map are reported below. Garnet is given both as the total volume of garnet and as four distinct zoned domains (Grt_C = core; Grt_M = mantle; Grt_R = rim; Grt_{S+N} = secondary and neoblastic garnet).

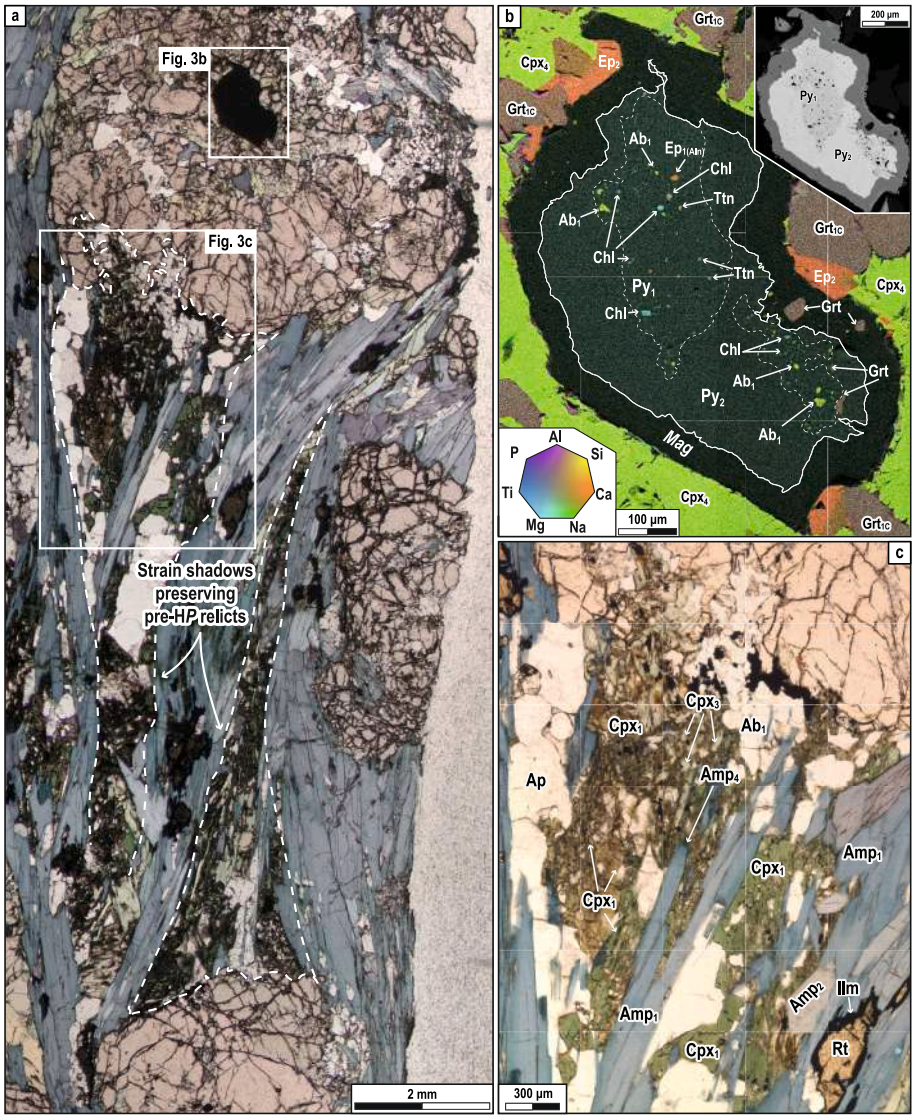

Fig. 3. a) PPL photomicrograph of the microdomain of section GP21-1F where some pre-H*P* relicts can be observed. b) Combined multi-elemental chemical map of the zoned pyrite grain included at the centre of a garnet porphyroblast. Here small inclusions of chlorite, albite, garnet, epidote, allanite, and titanite can be observed. For an additional example of zoned pyrite, see Supplementary Fig. 3a. c) Garnet strain shadows showing pre-kinematic relicts of albite, apatite, and deep-green clinopyroxene overgrown by syn-Dp Cpx_3 and Amp_1. (For interpretation of the references to colour in this figure legend, the reader is referred to the web version of this article.)

alternating amphibole- and clinopyroxene-rich levels that wrap around large garnet porphyroblasts (up to 1 cm in size; see Fig. 2a for section GP21-1B). The mapped sample GP21-1B consists of garnet (33.2 vol%), amphibole (31.4 vol%), clinopyroxene (22.4 vol%), apatite (5.2 vol%), rutile (2.5 vol%), albite (1.9 vol%), ilmenite (1.0 vol%), quartz (0.8 vol %), magnetite (0.7 vol%), epidote (0.4 vol%), pyrite (0.3 vol%), titanite (0.2 vol%) and lamellae of paragonite (Fig. 2b). Three main multi-stage blastesis-deformation events can be distinguished, i.e., a pre-Dp event (i.e., earlier than the principal deformation event), in turn consisting of a pre-H*P* stage and an H*P* pre-Dp stage, a syn-Dp event and a post-Dp event (Fig. 4a), which will be further detailed in the following sections. The early and late pre-Dp events and the Dp event develop a metamorphic foliation. The mineral assemblage related to the Dp event is defined by garnet + Na-amphibole + clinopyroxene + quartz + apatite + rutile + pyrite.

The effective bulk rock composition (EBC I; Table 1) and the coarse-grained nature of the sample suggest that the protolith was a Fe-Ti gabbro with very high Fe concentrations (Supplementary Fig. 2), among the highest ever reported for the Fe-Ti metagabbros outcropping in the Western Alps.

3.5. *Pre-Dp stages*

3.5.1. *Pre-HP stage*

Sample GP21-1F shows relict evidence of a pre-H*P* event (Fig. 4a). As shown in Fig. 3a and in Supplementary Fig. 3, such evidence can be found (i) within two pyrite grains that acted as a tectonic capsule, the first included at the centre of a garnet (Fig. 3b) and the second one aligned along the main foliation, and (ii) within the strain shadows of two garnet crystals (Fig. 3a, c), one of which is also the host of the first pyrite grain (Fig. 3b). Both pyrites display a patchy and corroded (embayed) core (Py_1) characterized by multiple inclusions of albite (Ab_1), chlorite, titanite, epidote + allanite (grouped as Ep_1), quartz and clinopyroxene (Cpx_1). Host pyrite contamination prevents us from obtaining reliable quantitative compositions. The pyrite core is overgrown by mostly inclusion-free euhedral pyrite (Py_2; Fig. 3b; Supplementary Fig. 3): rarely, Py_2 includes H*P* minerals like rutile, glaucophane and omphacitic clinopyroxene (as defined below). Both are

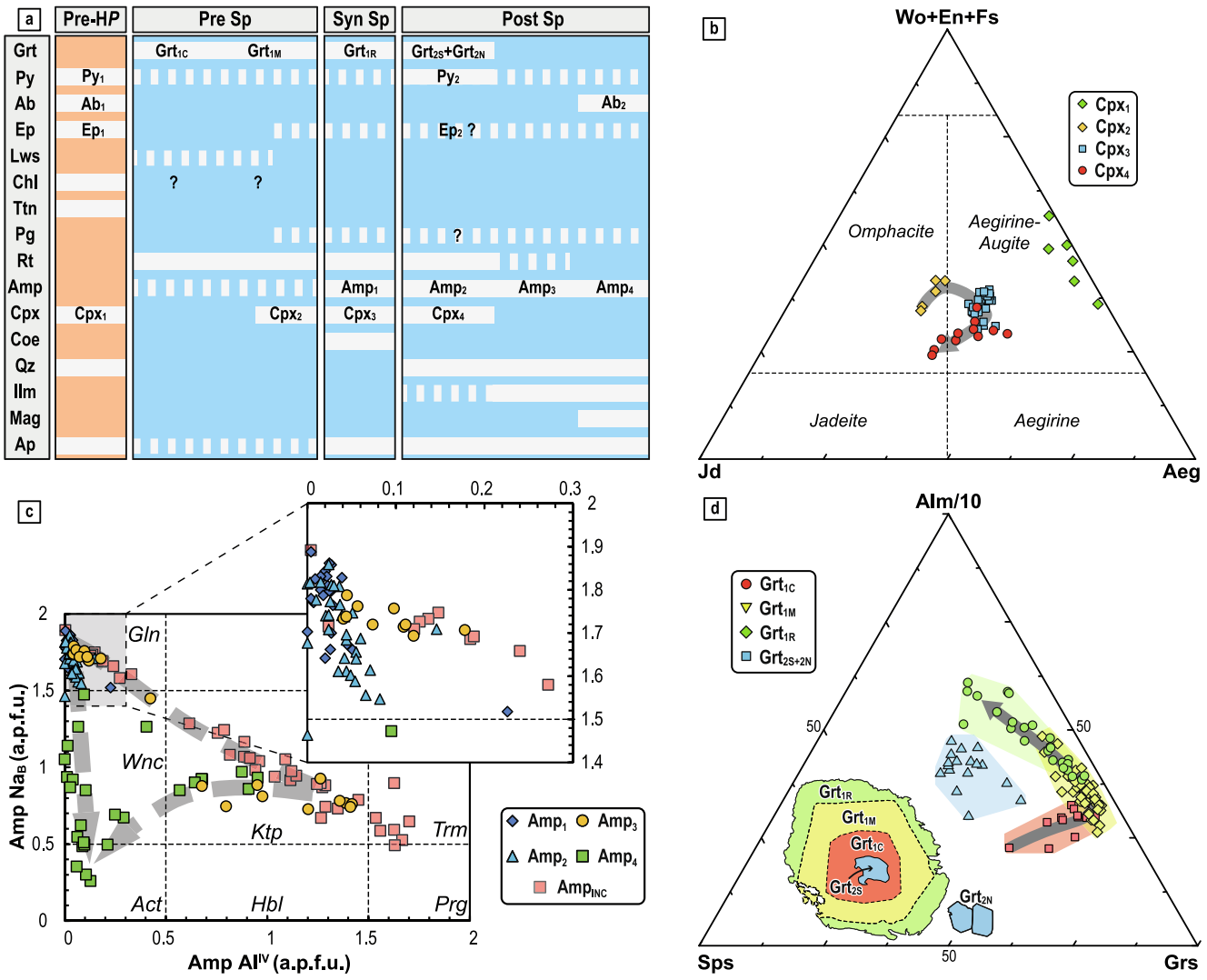

Fig. 4. a) Blastesis-deformation relations for the studied sample. b) Pyroxenes' compositions plotted in the ternary diagram after Morimoto (1988); c) Compositional diagram for amphiboles according to the classification of Leake et al. (1997); d) Triangular plot for garnet end-members allowing discrimination between primary and secondary garnet.

pseudomorphosed by magnetite rims, likely due to atmospheric oxidation and alteration. Garnet strain shadows host relicts of albite, apatite, and deep-green twinned clinopyroxene. Albite has less than 2 % of anorthitic component (Ab_1; Supplementary Fig. 4a; Supplementary Table 1), while clinopyroxene (Cpx_1) is strongly depleted in Al and falls in the aegirine-augite field close to the augite-aegirine join (Fig. 4b; Table 2). Moreover, both Ab_1 and Cpx_1 are overgrown by randomly oriented small pale-green omphacitic clinopyroxene (Fig. 3c) and acicular deep-blue Fe-glaucophane that mark the Dp (i.e., Cpx_3 and Amp_1, respectively, see explanation below). Such microstructural observations, coupled with the characteristic mineral associations, indicate that, in the studied samples, some relict evidence of a pre-H*P* history escaped complete re-equilibration.

3.5.2. *Pre-Dp stage*

The pre-Dp event foresees the blastesis of garnet cores and mantles (Grt_{1C} and Grt_{1M}, respectively; Fig. 4d, 5 and 6), thus defining an early pre-Dp and a late pre-Dp stage. Both garnet core (Grt_{1C}) and mantle (Grt_{1M}) are mostly almandine with average compositions of: (i) Grt_{1C} = $Alm_{70}Grs_{16}Prp_6Sps_4Andr_4$; and (ii) Grt_{1M} = $Alm_{75}Grs_{13}Prp_7Sps_2Adr_3$ (Fig. 5a-d; Table 2). Chemical profiles and maps show that Grt_{1C} is characterized by a continuous decrease of *X*Ca (0.25–0.16) and *X*Mn (0.08–0.02), counterbalanced by an increase of *X*Fe (0.61–0.75), whereas *X*Mg is rather flat (0.05–0.10) (Fig. 5a-d; 6). Grt_{1M} is characterized by roughly flat chemical profiles of *X*Ca (0.12–0.20), *X*Mn (0.01–0.05), *X*Fe (0.72–0.79), and *X*Mg (0.02–0.11) (Fig. 5a-d; 6). In chemical maps, Fe and Mn reveal a patchy distribution (Fig. 5c, d). Both Grt_{1C} and Grt_{1M} include apatite and rutile (Fig. 2b). Blue to deep green amphibole (Amp_{INC}) is included within Grt_{1C} or Grt_{1M}. However, this amphibole shows evidence of chemical interaction with the host garnet (Fig. 4c; Supplementary Table 1) and no reliable geothermobarometric constraints could be derived from it. Grt_{1M} also shows mineral inclusions defining concentric zoning. The inner Grt_{1M} displays polymineralic inclusions of paragonite and epidote (up to 100–150 μm; Fig. 7a; Supplementary Table 1). Epidote is zoned, with a zoisite core rimmed by a clinozoisite mantle and a Fe-rich epidote rim (Fig. 7a; *X*Zo decreasing from 0.84 to 0.16; Supplementary Figure, 4b, 5b, 5c). These paragonite + epidote inclusions in garnet have been interpreted as pseudomorphs after former lawsonite (e.g., Groppo and Castelli, 2010; Hamelin et al., 2018; Manzotti et al., 2022). The outer Grt_{1M} includes small pale-green clinopyroxene (Cpx_2; ranging from <90 μm up to 500 μm), locally extending into the garnet rim (Grt_{1R}; Supplementary Fig. 5b, c). These clinopyroxene inclusions display compositions in the omphacite and aegirine-augite fields (Fig. 4b) of Morimoto (1988), with *X*Na ranging

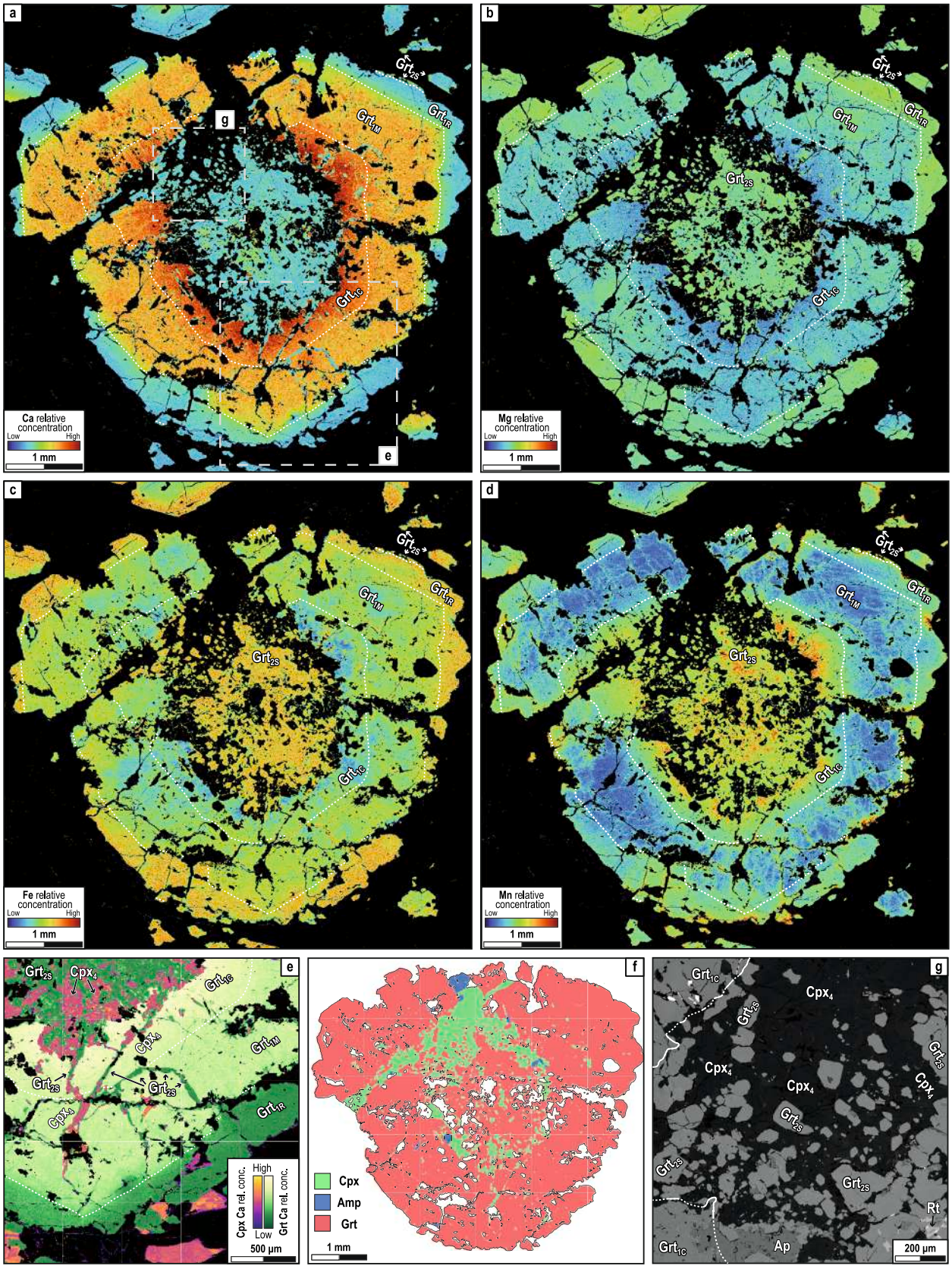

Fig. 5. a-d) Relative concentration X-ray maps of Ca, Mg, Fe and Mn in garnet. e) Ca relative concentration in clinopyroxene and garnet showing how fractures across Grt_{1C}, Grt_{1M} and Grt_{1R} are filled by intergrown Grt_{2S} and Cpx_4. f) Classified map showing the distribution of clinopyroxene and amphibole within garnet. g) Back-scattered image of a micro-site in the core of the same garnet reported in (a)-(d), showing the skeletal intergrowth of Cpx_4 + Grt_{2S} replacing the former Grt_{1C}.

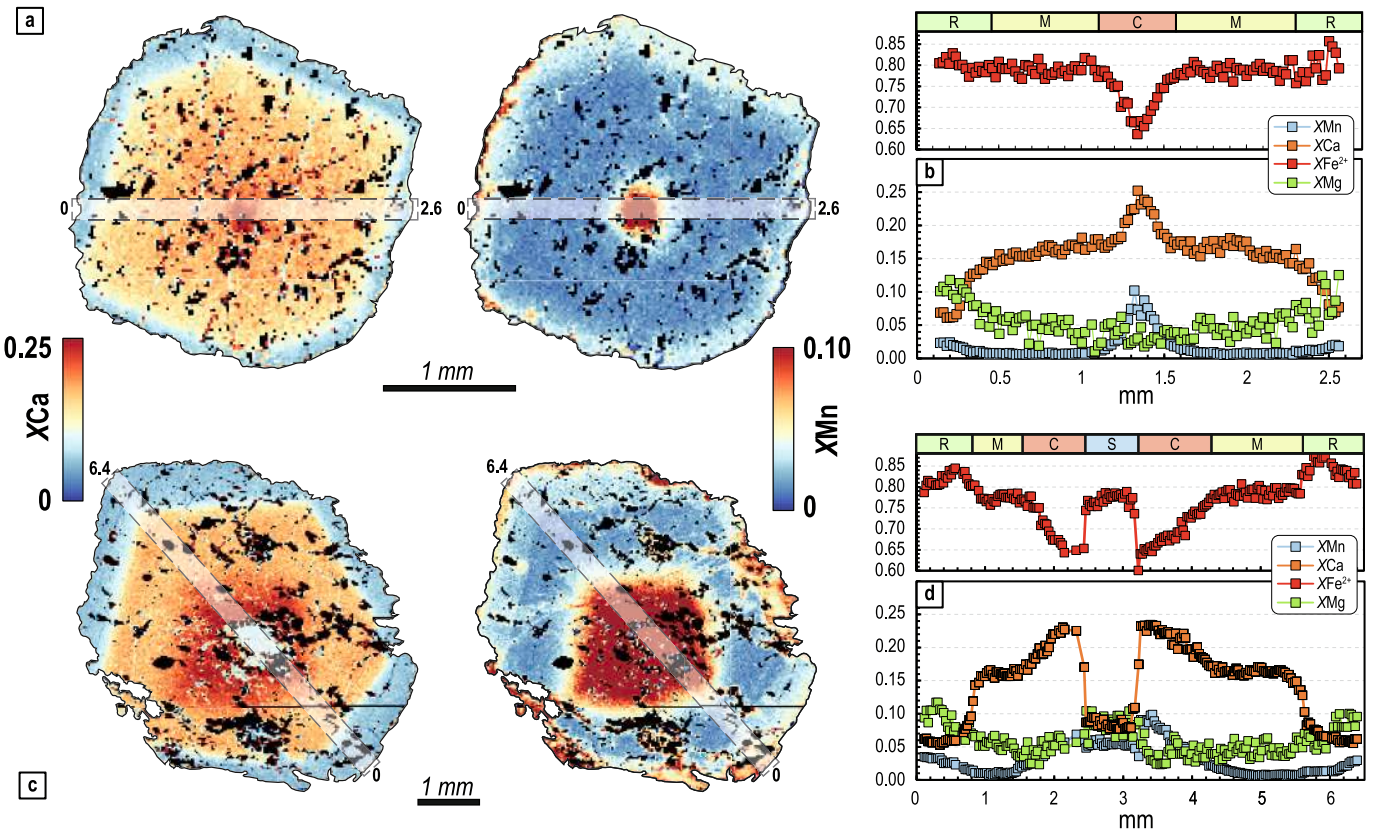

Fig. 6. a, c) *X*Ca (left) and *X*Mn (right) calibrated maps of two garnet porphyroblasts. b, d) Chemical profiles across the same garnet crystals reported in (a) and (c). (c) and (d) refer to an atoll garnet porphyroblast.

between 0.60 and 0.68 (Table 2).

3.6. Dp stage

The Dp event is defined by the blastesis of garnet rims (Grt_{1R}; Fig. 2b, 5, 6a, c) on previous garnet mantles. Garnet rims are mostly almandine with an average composition Grt_{1R} = $Alm_{79}Grs_6Prp_{10}Sps_2Andr_3$ (Table 2). Chemical profiles and maps reveal a sharp mantle-rim transition, defined by a decrease in *X*Ca (0.15–0.06) and an increase in *X*Mg (0.07–0.13) and *X*Fe (0.76–0.84; Fig. 6b, d). On the other hand, *X*Mn (0.01–0.04) describes a gentler and continuous increase from the mantle to the rim. In the matrix, dark blue acicular amphibole (Amp_1; Fig. 7b) and small and elongated bright green clinopyroxene (Cpx_3; Fig. 7c-f) are aligned sub-parallel to each other. They envelop the garnet porphyroblasts and define, together with abundant apatite and rutile, the main Sp foliation. Amp_1 is glaucophane to Fe-glaucophane with Na_B between 1.52 and 1.89 a.p.f.u., Al^{IV} between 0 and 0.25 a.p.f.u. and with *X*Na ranging between 0.84 and 0.96 (Fig. 4c; Table 2). Amp_1 is also found within garnet strain shadows and included within Grt_{1R}. Cpx_3 is an aegirine-augite (Fig. 4b; Table 2) according to the classification of Morimoto (1988), similar to Cpx_2 but with slightly higher *X*Na values (0.62–0.68). Locally, granoblastic quartz aggregates occur in the garnet strain shadows, and pyrite (Py_2) occurs oriented along the Sp. Rutile crystals are observed along the Sp and included within garnet porphyroblasts, amphibole, clinopyroxene and pyrite; they are characterized by ilmenite lamellae cross-cutting single rutile crystals.

Finally, whole section chemical mapping indicated the presence of small and rare SiO_2 inclusions within the garnet rims (Grt_{1R}; Fig. 8a). Such inclusions (Fig. 8b, c) are 1–20 μm (Fig. 8b, c) sized monocrystalline grains surrounded by garnet (few tens of micrometers below the section surface). They occur either in clusters (Fig. 8b) or as isolated ones (Fig. 8c). Some inclusions exhibit well-developed facets, while most of them show a more rounded shape and sometimes with re-entrant angles (Fig. 8b, c). Raman microspectroscopic analyses (performed on a 100 μm thick section) identified such inclusions as coesite on the base of their characteristic spectrum (Boyer et al., 1985). The Raman spectra of coesite show the main vibrational mode at 523 cm^{-1} (instead of 521 cm^{-1}), the secondary bands are at 124, 150, 181, 206, 270, 325, 354, 426, 471, 791, 820, 843, 1038, 1148, 1168 cm^{-1}. The intensity of the peaks changes depending on the orientation of the inclusion measured (Fig. 8d). Some peaks show a shift of a few cm^{-1}. No quartz inclusions in garnet were found. Rare inclusions of coesite display radial cracks in the surrounding garnet.

3.7. Post-Dp stage

Chemical profiles and maps, together with microstructural observations, reveal the existence of a sharp and corroded (embayed) boundary within garnet porphyroblasts, whose core has been put in communication with the surrounding matrix by fracturing and dismembering. This sharp boundary is also marked by peculiar skeletal intergrowths between garnet and green clinopyroxene (Fig. 5e-g). These microstructures suggest the presence of a second generation of garnet replacing the early garnet cores (Grt_{1C}). This secondary garnet (Grt_{2S}) differs from Grt_{1C} for the sharp drop in *X*Ca and increase in *X*Fe observable both in chemical maps (Fig. 5a-d, 6c) and chemical profiles (Fig. 6d). Additionally, small garnet neoblasts (Grt_{2N}), chemically identical to Grt_{2S}, are observed locally along the main foliation (Figs. 2b, 7f). Both Grt_{2S} and Grt_{2N} have an average composition of Grt_{2S+2N} = $Alm_{76}Grs_6Prp_{10}Sps_5Adr_3$ (i.e., *X*Ca = 0.06–0.13, *X*Mn = 0.04–0.12, *X*Mg = 0.05–0.12, *X*Fe = 0.70–0.80; Table 2) and differ from Grt_{1R} for the general decrease in *X*Fe, the increase in *X*Mn and slightly higher *X*Ca values (Fig. 5b, 6d).

Randomly oriented prismatic and euhedral dark-blue amphibole

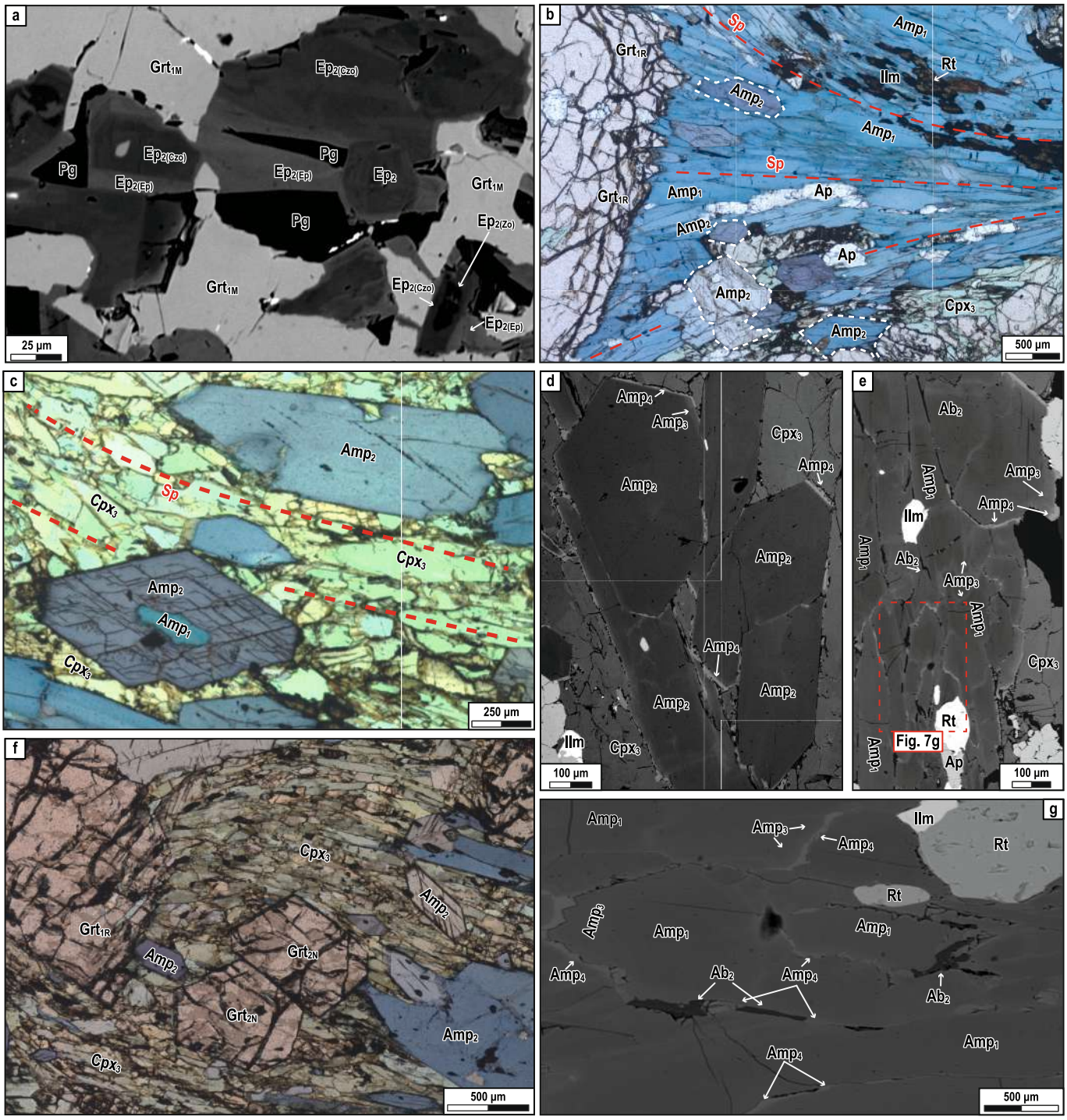

Fig. 7. a) Back-scattered electron image (BSE) of polymineralic inclusions within Grt_{1M}, consisting of epidote (zoisite core, clinozoisite mantle and epidote rims) and paragonite and interpreted as pseudomorphs after lawsonite. b) Sp foliation defined by the isorientation of Amp_1 and Cpx_3, overgrown by Amp_2. Rutile crystals along the Sp are rimmed by ilmenite. c) Detail of Sp foliation marked by Cpx_3 and euhedral post-kinematic Amp_2 statically overgrowing the Sp mineral assemblage. A detail of Amp_2 substituting Amp_1 is also visible (PPL). d, e) BSE images showing details of Amp_3 and Amp_4 thin rims growing on Amp_2 blasts. f) Grt_{2N} neoblasts growing on the Sp foliation (PPL). g) Interstitial Ab_2 growing between Amp_{3-4} blasts (BSE).

crystals (up to 3 mm in size) statically overgrow the main foliation (Amp_2; Fig. 7b-f). They include Cpx_3, Amp_1, and rutile. Amp_2 displays glaucophane to Fe-glaucophane composition, with Na_B between 1.46 and 1.86 a.p.f.u., Al^{IV} between 0 and 0.15 a.p.f.u. and with XNa ranging between 0.81 and 0.96 (Table 2). Amp_1 and Amp_2 are therefore overlapped in composition (Fig. 4c). Two additional types of green amphiboles (Amp_3 and Amp_4) occur as thin rims around both Amp_1 and Amp_2 (Fig. 7d, e, g), showing a wide range of compositions. Amp_3 is characterized by Na_B between 1.79 and 0.73 a.p.f.u. and Al^{IV} between 0.04 and 1.42 a.p.f.u., and generally plots over a wide compositional space (Fig. 4c), from the glaucophane to the katophorite field (Leake et al., 1997). Amp_4 is characterized by Al^{IV} values lower than 0.95 a.p.f.u., and Na_B between 0.26 and 1.74 a.p.f.u., hence plotting in the winchite and actinolite fields. Amp_4 describes two distinct chemical trends depending on which amphibole they are growing from (i.e., Amp_1/Amp_2 vs. Amp_3) (Fig. 4c). Small, interstitial albite grows among these

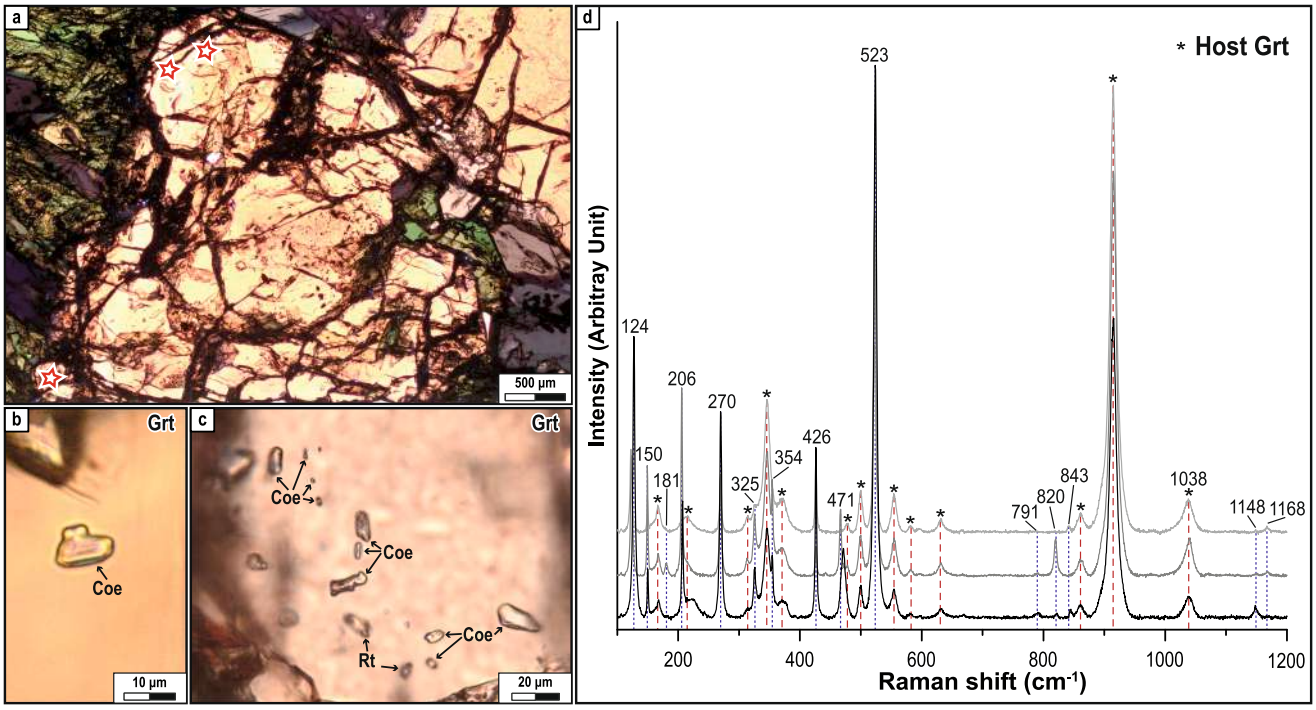

Fig. 8. a) PPL photomicrograph of the thick section of a coesite-bearing garnet. Red stars mark coesite inclusions found in the garnet rim. b, c) PPL photomicrograph of coesite and rutile inclusions in garnet rims. (c) is a focus stack composite PPL photomicrograph produced to better portray an inclusion cluster of coesites and rutiles. d) Representative Raman spectra of coesite inclusions and of the host garnet (whose vibrations are marked by asterisks). (For interpretation of the references to colour in this figure legend, the reader is referred to the web version of this article.)

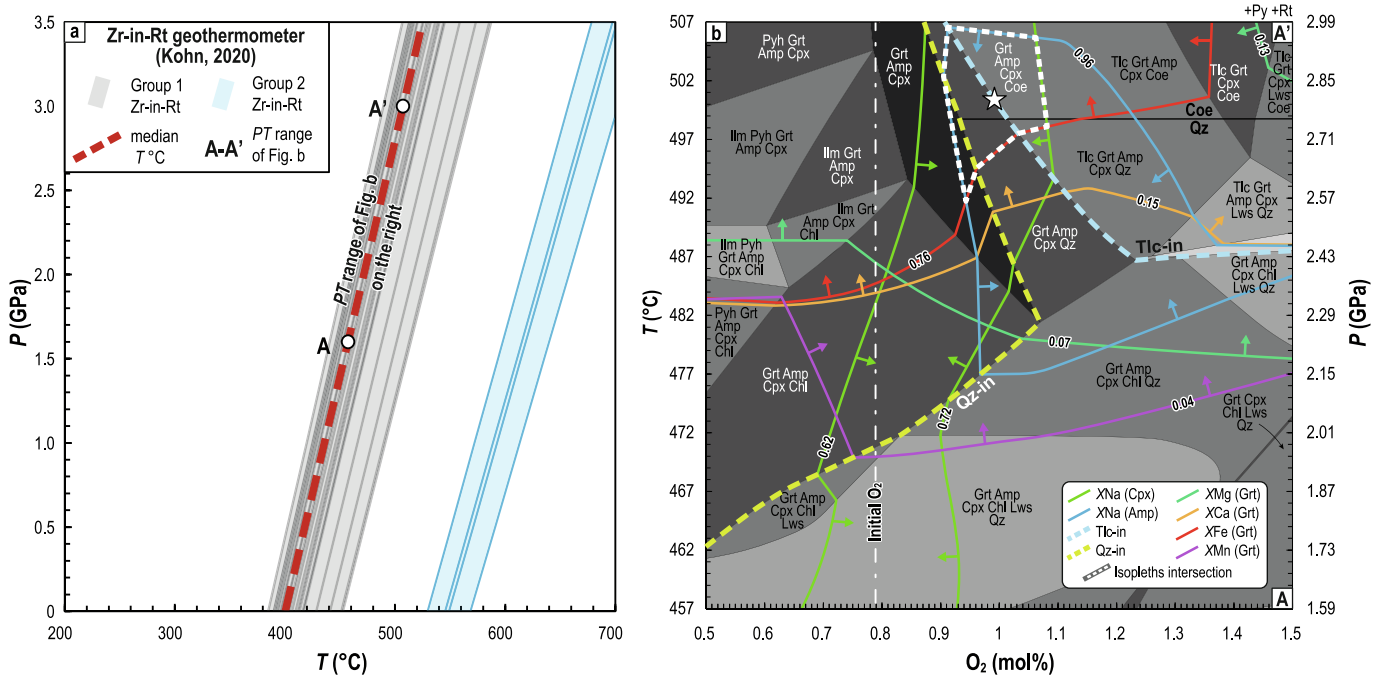

Fig. 9. a) *P–T* diagram showing the calculated Zr-in-rutile temperatures for the two compositional groups, with the median temperature in red. b) *T*(*P*)-O_2 compositional phase diagram contoured with garnet (Grt_{1R}), clinopyroxene and amphibole isopleths, used to estimate the O_2 bulk amount for the subsequent isochemical phase diagram calculations. Arrows on isopleth pairs define the compositional ranges observed for each mineral phase, pointing toward the inside of the compositional range in this and in the following phase diagrams. The dashed-dotted line indicates the initial stoichiometric-determined O_2 and the white star indicates the chosen corrected O_2 value. (For interpretation of the references to colour in this figure legend, the reader is referred to the web version of this article.)

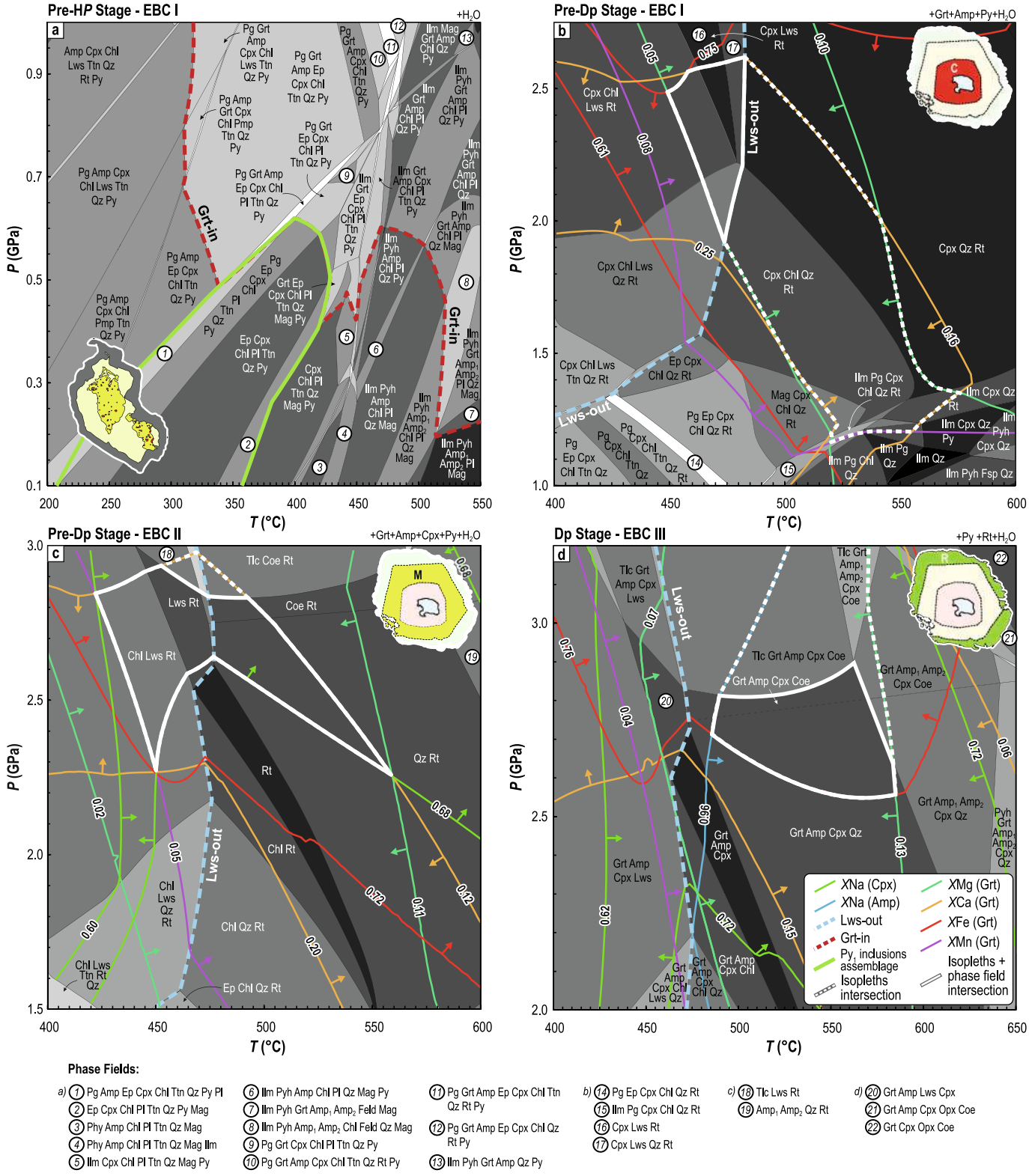

Fig. 10. Isochemical phase diagrams modelled for different metamorphic stages. a) The pre-H*P* stage is defined by the mineral association within pyrite cores (EBC I). b) Early pre-Dp stage contoured for the Grt_{1C} isopleths (EBC I). c) Late pre-Dp stage contoured for the Grt_{1M} and Cpx_2 isopleths (EBC II). d) syn-Dp stage contoured for the Grt_{1R}, Cpx_3 and Amp_1 isopleths (EBC III). Arrows on isopleth pairs in (b), (c) and (d) define the compositional ranges observed for each mineral phase, pointing toward the inside of the compositional range.

last amphibole crystals (Ab_2; Fig. 7g). During this last event, rutile crystals along the main foliation and those reached by fractures within the host garnet are rimmed by ilmenite (Fig. 3c, 7b, g).

4. Geothermobarometry and thermodynamic modelling

4.1. Zr-in-rutile results

Rutile is observed in different microstructural positions, i.e., both included in all garnet domains and along the Sp foliation together with omphacite, glaucophane and apatite (Supplementary Fig. 5). The presence of quartz and zircon in the mineral assemblage assures that the activity constraints on Si, Ti and Zr, required by the Zr-in-Rt thermometer, are met (Kohn, 2020). After grinding, ca. 120 grains were separated and mounted, and their core was exposed by polishing. Of these, 15 were selected after careful inspection of the SEM and ablation results, to avoid contamination by inclusions, ilmenite lamellae and fractures. These analyses were supplementing 18 in situ analyses (performed on a 100 μm thick section) performed on rutile both included in garnet and along the Sp. Two groups have been distinguished based on Zr concentrations: the first has Zr between 15 and 48 ppm and coincides with rutile grains both along the main foliation (Sp) and those included in garnet; the second, with just four analyses, has Zr between 153 and 251 ppm (Supplementary Table 1). For temperature estimation, the *P*-sensitive formulation of Kohn (2020) has been used in the pressure range 0–3.5 GPa, with a 0.5 GPa step; the results are reported in Supplementary Table 1 and Fig. 9a. The median temperature of the first group at 1.5 GPa is (with 2σ) 454 ± 31 °C, while at 3.0 GPa is 507 ± 34 °C. The second group records higher temperatures, at 1.5 GPa = 614 ± 30 °C and at 3.0 GPa = 679 ± 32 °C.

4.2. Estimating the bulk O_2

Since the GP21-1B rock composition is characterized by the presence of redox-sensitive sulfur and by a peculiarly high Fe content, the effective bulk O_2 must be properly constrained. A *T*(*P*)-O_2 compositional phase diagram has been therefore calculated along a *T*(*P*) gradient defined by the equation that describes the Zr-in-Rt median temperature values (dashed bold red line in Fig. 9a). EBC III and the compositions of the syn-Dp minerals have been used as input data for the modelling. The bulk O_2 has been constrained based on the intersection of the compositional isopleths modelled for the syn-Dp assemblage (Fig. 9b). The initial O_2 derived from the mass-balance calculations was corrected accordingly (i.e., increased by ~23.4 %). The same correction was applied to the other two effective EBCs.

4.3. P–T isochemical phase diagrams

Five isochemical phase diagrams have been calculated in different *P*–*T* ranges using the three effective EBCs discussed above (Figs. 10, 11) and reported in Table 1. All the phase diagrams are dominated by three- to six-variant fields with a few seven-variant fields at H*P* conditions. The phase diagram calculated with the unfractionated EBC I at low *P*–*T* conditions (Fig. 10a) predicts that the mineral association found as relicts in Py_1 cores (Ab_1 + Ep_1 + Chl + Cpx_1 + Qz + Ttn) is stable in a positively sloped *P*–*T* region below ~0.6 GPa and between ~200 and ~430 °C (delimited by the bold light green line in Fig. 10a). The garnet-in phase boundary is observed only in the low *P*–*T* phase diagram in Fig. 10a. Garnet is stable above ~350 °C and above 0.5–0.6 GPa at blueschist-facies conditions, while at amphibolite-facies conditions is stable above ~500 °C (Fig. 10a). Altogether these pieces of thermodynamic evidence qualitatively constrain such an event at prehnite-pumpellyite- to greenschist-facies conditions (pre-H*P* stage).

The unfractionated EBC I was used to model the growth of the garnet

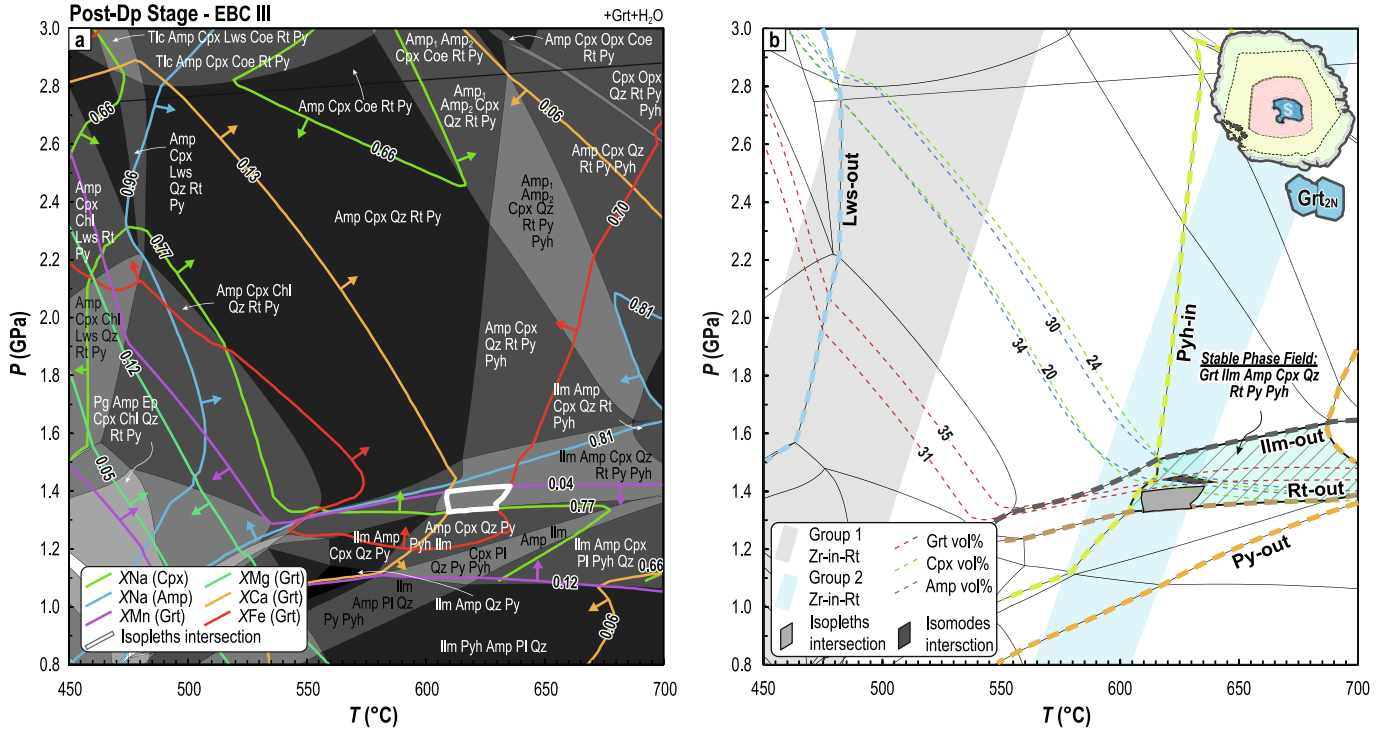

Fig. 11. a) Isochemical phase diagram for the post-Dp stage, contoured for the Grt_{2S} + Grt_{2N}, Cpx_4 and Amp_2 isopleths. Arrows on isopleth pairs define the compositional ranges observed for each mineral phase, pointing toward the inside of the compositional range. b) Same phase diagram as in a (with just the phase field boundaries for simplicity) where the Grt, Cpx and Amp isomodes (whose complete data computed in the P-T range of interest of this phase diagram are reported in Supplementary Fig. 6a, b, c), together with the Zr-in-Rt temperatures and the compositional isopleths intersection indicate that the last *P*–*T* conditions of rock equilibration are within the phase field Grt + Amp + Cpx + Py + Qz + Rt + Ilm + Pyh that is marked by the striped field.

core (early pre-Dp stage), whereas the fractionated EBC II was used to model the growth of the garnet mantle (late pre-Dp stage). The early pre-Dp mineral assemblage (Grt_{1C} + Lws ± Amp ± Chl + Rt + Py_1; Fig. 4a) is modelled in a narrow *P–T* interval at ~450–480 °C, ~2.2–2.7 GPa (Fig. 10b); a small amount of clinopyroxene (<5 vol%) is predicted to be stable in this field, but it was not observed in the sample. The modelled isopleths corresponding to the composition of Grt_{1C} converge in this field. The late pre-Dp mineral assemblage (Grt_{1M} ± Lws ± Amp + Cpx_2 + Rt + Py_1; Fig. 4a) is modelled in a wide *P–T* interval between ~420–510 °C and ~ 2.3–3.0 GPa (Fig. 10c); quartz/coesite are predicted to be stable in this field, although they were not observed in this shell of the garnet (Grt_{1M}); however, their predicted modal amount is very low. Notably, the occurrence of lawsonite pseudomorphs in the inner Grt_{1M} but not in the outer Grt_{1M} suggests that the Lws-out boundary was crossed during the growth of Grt_{1M}. The modelled isopleths corresponding to the compositions of Grt_{1M} and omphacitic clinopyroxene (Cpx_2) included in the outer Grt_{1M} converge in the *P–T* range of ~420–510 °C and ~ 2.3–2.9 GPa.

The Dp stage was modelled using the fractionated EBC III. The relatively large field corresponding to the observed syn-Dp assemblage (Grt_{1R} + Amp_1 + Cpx_3 + Qz/Coe + Rt; Fig. 4a) is further constrained by the intersection of the compositional isopleths modelled for garnet rim (Grt_{1R}), omphacitic clinopyroxene (Cpx_3) and glaucophane (Amp_1). These isopleths define a further increase in both temperature and pressure up to ~490–580 °C, ~2.5–2.9 GPa (Fig. 10d). The occurrence of coesite inclusions within the Grt_{1R} domain indicates that a minimum *P* of 2.75 GPa was reached by the studied rock.

Finally, the post-Dp stage was modelled using again the unfractionated EBC I (Fig. 11). This choice is justified by the fact that Grt_1 was pervasively fractured before the growth of Grt_{2S} and Grt_{2N}; this process exposed the Grt_1 core and mantle to the matrix, re-opening the system and making them again available to participate in metamorphic reactions. The post-Dp mineral assemblage (Grt_{2S+2N} + Amp_2 + Cpx_4 + Qz + Ilm + Rt + Py) is modelled in a relatively small *P–T* range at ~600–700 °C, ~1.3–1.6 GPa. Pyrrhotite is predicted to be stable at these conditions, although it was not observed in the sample; however, its predicted modal amount is very low. The compositional isopleths modelled for Grt_{2S} and Grt_{2N} barely overlap in this field (*X*Mg is especially poorly matching), whereas those of Cpx_4 and Amp_2 converge in this field at ~610–635 °C, ~1.3–1.4 GPa; Fig. 11a). The discrepancy between the measured and modelled Grt_2 compositions suggests that the EBC I used for the modelling does not perfectly reflect the true effective bulk composition during Grt_2 growth, i.e., that although the system was re-opened through Grt_1 fracturing, Grt_1 did not participate as a whole to the metamorphic reactions at this stage. As an additional qualitative constraint, the modelled mineral isomodes of garnet, clinopyroxene and amphibole are predicted to intersect within the post-Dp phase assemblage field (i.e., at ~615–640 °C and ~ 1.4 GPa; complete mineral volume data reported in Supplementary Fig. 6a, b, c). Notably, the second group of Zr-in-Rt temperatures (see above) suggests temperatures of 614 ± 30 °C at 1.5 GPa (Fig. 11b), overlapping with the *P–T* conditions defined by the post-Dp assemblage.

5. Discussion

5.1. Metamorphic evolution

The preserved prograde to peak mineral assemblage allowed us to reconstruct the poly-phasic metamorphic evolution of the studied coesite-glaucophane-bearing eclogite.

5.1.1. Pre-Dp stages

The mineral assemblages and textures observed in thin section GP21-1F provide valuable insights to reconstruct its early metamorphic history. The preservation of a low *P–T* mineral assemblage in strain shadows (Fig. 3a, c) and in pyrite grains included within garnet cores (Fig. 3b) suggests that this assemblage may be a relict of an early metamorphic (pre-H*P*) event (Fig. 4a). This is testified by the occurrence of albite and jadeite-free aegirine-augitic clinopyroxene in garnet strain shadows, both overgrown by omphacitic clinopyroxene (Cpx_3) and Fe-glaucophane (Amp_1). The role of low-strain domains in preserving mineral assemblages and compositions from re-equilibration at H*P* conditions has been recently discussed by Chapman et al. (2019), who observed that up to 32 % of an eclogitized metagabbro was constituted by low-strain domains where primary magmatic mineral assemblage and microstructures escaped H*P* metamorphism. The *P–T* conditions modelled for this pre-H*P* stage (i.e., <400 °C, <0.6 GPa; Fig. 12a) are compatible with a lower oceanic crust environment, as envisioned by recent field and geochronologic data from De Togni et al. (2024), where the protolith gabbro intrusion has been dated at ~150 Ma. The occurrence of chlorite and epidote suggests that a major hydration event might have occurred at very low- to low temperature conditions (i.e. from prehnite-pumpellyite to greenschist-facies conditions), providing the H_2O necessary to develop the observed hydrous H*P* mineral assemblage during the following subduction. Furthermore, jadeite-free aegirine-augitic clinopyroxene similar to that observed in the pre-Dp stage has been reported from hydrothermally altered and oxidized basic rocks of the oceanic crust metamorphosed at prehnite-pumpellyite facies conditions (<250 °C, <0.6 GPa) at the onset of subduction (Tsujimori and Liou, 2007 and references therein).

The early pre-Dp stage is the first record of H*P* metamorphism in the studied rock; this has been constrained at ~450–480 °C, ~1.9–2.6 GPa, in the lawsonite stability field. At such conditions, the growth of the garnet core (Grt_{1C}) is modelled to be mostly related to the chlorite breakdown at $T > 470$ °C and $P > 2.1$ GPa (Fig. 12a; Supplementary Fig. 5). The late pre-Dp stage, with the growth of the garnet mantle (Grt_{1M}), records the transition from lawsonite-blueschist facies conditions to eclogite-facies conditions at ~420–510 °C and ~ 2.3–2.9 GPa. Notably, the modelled breakdown of lawsonite seems to occur at temperatures approximately 100–150 °C lower in the used Fe-rich and Ca-poor effective bulk rock composition compared to more typical mafic rock compositions (e.g., Tsujimori and Ernst, 2014). We suggest that the low Ca activity and the high Fe activity of sample GP21 might have restricted the stability field of Lws in favour of an enlarged stability field of eclogitic Fe-rich garnet. The transition from blueschist- to eclogite-facies is generally considered a major dehydration step for the downgoing plate. The results of the modelling predict that the lawsonite breakdown might have been the last major dehydration event experienced by the studied rock, as glaucophane is predicted to remain stable up to 600–650 °C and > 3.0 GPa (and indeed, a high modal amount of glaucophane does occur in the studied eclogite; Supplementary Fig. 6d). This is in line with the conclusions of Manzotti et al. (2020), who showed that in Fe-rich rocks, glaucophane stability is expanded at higher *P–T* compared to Fe-poorer systems. Furthermore, an expanded glaucophane stability field might also reflect an initially high water content (e.g., (Angiboust and Agard, 2010).

5.1.2. Dp stage

The Dp stage is defined by: (i) the growth of garnet rim (Grt_{1R}) including coesite, and (ii) the main Sp foliation which is marked by dark blue acicular amphibole (Amp_1) and small and elongated bright-green clinopyroxene (Cpx_3; Fig. 3a). The *P–T* conditions recorded by this assemblage lie between ~480–580 °C and ~ 2.75–2.9 GPa, (Fig. 12a). The *P–T* conditions constrained for both the pre-Dp and Dp stages are consistent with Zr-in-rutile estimated temperatures. The first group of rutile grains returns median temperatures (with 2σ) of 454 ± 31 °C at 1.5 GPa and 507 ± 34 °C at 3.0 GPa (grey field in Supplementary Fig. 6d). The excellent agreement between forward thermodynamic modelling and conventional thermometry (e.g., Hernández-Uribe et al., 2024) confirms the reliability of these *P–T* constraints, especially of the H*P* metamorphic peak.

Overall, the delineated prograde *P–T* path suggests that a substantial

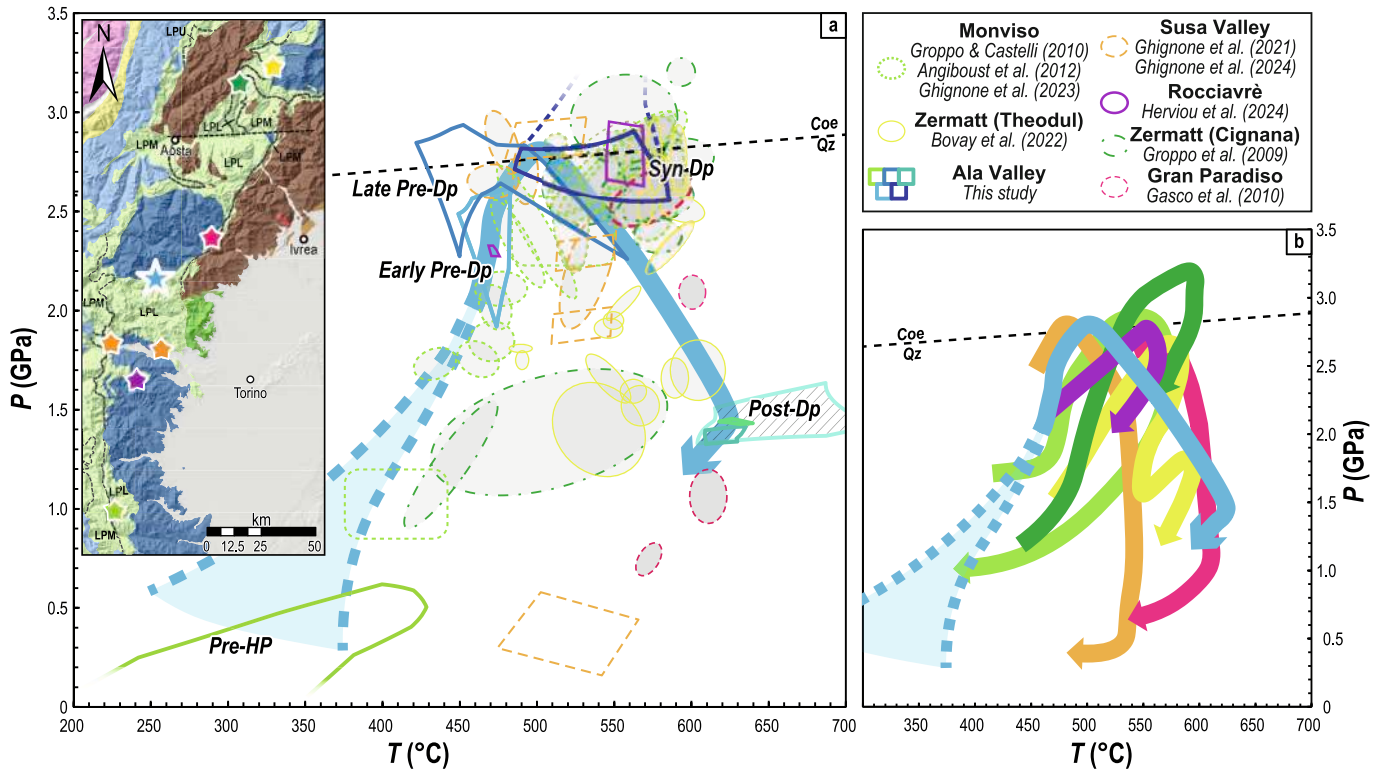

Fig. 12. a, b) Location, *P–T* estimates and paths of other mafic eclogites in or near the LPL compiled from the literature. Legend colour coding is valid for both images.

P increase occurred during the pre-Dp stage, whereas a more pronounced heating ($\Delta T \sim 80$ °C) occurred at peak UH*P* conditions. This might indicate that the studied rock may not have been thermally re-equilibrated before peak pressure. Peak pressure conditions inferred for the LPL in the Ala Valley (480–580 °C, ~2.75–2.9 GPa) point to a remarkably higher peak pressure compared to those of Sandrone et al. (1986), but are in excellent agreement with the revised estimates of Herviou et al. (2022), who report a *P–T* peak of 500–580 °C, 2.2–2.8 GPa for the LPL.

5.1.3. Post-Dp stage

The post-Dp stage encompasses several distinct events. The first is represented by the fracturing and dismembering of garnet porphyroblasts and the dissolution of their cores, followed by the growth of a new garnet generation (Grt_{2S}), skeletally intergrown with omphacitic Cpx_4 (i.e., atoll garnet formation, see below). This second event is also accompanied by the static blastesis of large euhedral glaucophane Amp_2 (Fig. 7b, c) and smaller garnet (Grt_{2N}) neoblasts in the rock matrix (Fig. 7f). Forward thermodynamic modelling, qualitatively supported by Zr-in-Rt thermometry, allow constraining this post-Dp blastesis event at around 600–630 °C, 1.3–1.5 GPa, during heating decompression, still at eclogite-facies conditions (Fig. 12a; Supplementary Fig. 6d). This implies that the fracturing and dissolution of garnet porphyroblasts should also have occurred at eclogite-facies conditions. Notably, such *P–T* conditions are close to the modelled Py-out reaction (Fig. 11b). This observation could explain the observed pyrite zoning as due to the consumption of Py_1 during heating decompression (i.e., crossing the Pyh-in reaction up-*T*) followed by the growth of Py_2 during cooling decompression (i.e., crossing again the Pyh-in, reaction in the opposite direction), and the concomitant inclusion of eclogite-facies minerals like rutile, glaucophane, and omphacite. It is also worth noting that the *P–T* conditions constrained for the post-Dp stage are similar to those reported by Bovay et al. (2022) and Hartmeier et al. (2024) in the Zermatt–Saas zone (i.e., 560 ± 30 °C and 1.6 ± 0.2 GPa).

Retrograde re-equilibration after this stage is only minor and testified by: (i) the static growth of two additional generations of green-amphibole (Amp_3 and Amp_4), rimming both Amp_1 and Amp_2 (Fig. 7g), and ranging in composition from glaucophane to katophorite (Amp_3) and from winchite to actinolite (Amp_4) (Fig. 4c); (ii) the growth of small albite (Ab_2) grains interstitial between these last amphibole crystals; (iii) the growth of ilmenite at the rim of rutile.

5.2. P–T comparison in the LPL

The obtained prograde *P–T* path is characterized by a steep increase in pressure ($\Delta P > 2.8$ GPa) for a $\Delta T \approx 200–250$ °C, indicating rapid burial with only minor thermal equilibration. This prograde evolution is comparable to what was previously reported for tectonic units in the same region in the Western Alps (Fig. 12a, b), e.g., Zermatt-Saas (e.g., Angiboust and Agard, 2010; Bovay et al., 2022; Groppo et al., 2009), Savoy-Susa and Cottian Alps (e.g., Ghignone et al., 2020, 2024; Plunder et al., 2012) and Monviso (e.g., Ghignone et al., 2023 and references therein; Groppo and Castelli, 2010; Locatelli et al., 2018) and Rocciavrè (Herviou et al., 2025). Also, the peak pressure conditions registered by the different eclogitic units of the Western Alps are identical (within the uncertainties: 29–42 °C and ± 0.2–0.3 GPa for mafic chemical systems at H*P* conditions; Hernández-Uribe et al., 2024) with the results obtained in this work (500–580 °C and 2.5–2.9 GPa). This suggests that subduction of the oceanic lithosphere to UH*P* conditions occurred with a relatively coherent evolution in the whole Western Alps (see Agard, 2021 for a review). In the LPL, UH*P* peak conditions have been reported so far for: (i) the Lago di Cignana UH*P* unit, wherein coesite was discovered by Reinecke (1998) and the occurrence of microdiamonds was reported by Frezzotti et al. (2011); (ii) a portion of the Zermatt-Saas unit, wherein Luoni et al. (2018) reported UH*P* conditions in Ti-chondrodite-bearing serpentinite and (iii) the Monviso and the Susa units in which coesite was recently discovered (Ghignone et al., 2023, 2024). Our finding of coesite is the first in the LPL sector around the

Gran Paradiso Massif which was the last sector around an Internal Crystalline Massif still lacking a coesite finding marking peak UH*P* conditions.

In the literature, the exhumation paths (i.e., after the peak-*P*) differ in different sectors of the LPL (Fig. 12b). In our case study, we observe a decompression coupled with a significant *T* increase from 500 to 550 °C to 600–630 °C (i.e., ΔT = 50–130 °C). However, it is important to highlight that the decompression heating constrained for this sector of the LPL is not a common feature of the whole LPL. In most LPL units, in fact, peak-*P* is followed by slight isothermal decompression, indicating that the tectonic units followed a rapid exhumation after decoupling from the descending slab (e.g., Rubatto and Hermann, 2001). Other authors, instead, invoke β-shaped *P*–*T* paths (Bovay et al., 2022; yellow arrow in Fig. 12b), whereas few predict a decompression heating similar to our path. Several mechanisms could explain this trajectory, including: (i) mantle delamination; (ii) multiple short-lived cycles of burial and exhumation associated with orogen-scale transitions between shortening and extensional deformation; (iii) coupling during exhumation between shallower, slightly cooler units and deeper, hotter units; and (iv) asthenospheric upwelling linked to slab rollback or crustal exhumation paired with slab breakoff. Further research is required to determine the extent and the origin of this significant heating during decompression and its tectonic implications, but it is outside of the scope of this paper.

5.3. Atoll garnet formation

5.3.1. Grt_{1C} dissolution and Grt_{2S} precipitation

Multiple models for atoll garnet development have been proposed throughout the years, depending on the metamorphic conditions and lithologies. The main models include (e.g., Cao et al., 2018; Faryad et al., 2010; Godet et al., 2022; Hartmeier et al., 2024; Kulhánek et al., 2021 and references therein): resorption and recrystallisation of garnet core, simultaneous multiple nucleation and coalescence, rapid and short-term poikiloblastic growth, matrix-dependent garnet growth, and fluid-garnet interaction due to crack-assisted fluid infiltration within garnet cores. In this case study, the following petrographic and mineral-chemical data can be best explained by the last model. (i) The sharp and corroded boundaries observed between the old garnet core (Grt_{1C}) and the new secondary garnet (Grt_{2S}; Fig. 5e) are most easily interpreted as dissolution features, likely caused by the involvement of a fluid phase. (ii) The fractures crosscutting Grt_{1C} and Grt_{1M}, filled with intergrown Cpx_4 and Grt_{2S} (Fig. 5e-g), along with the associated Fe and Mg patchy zoning in garnet (Fig. 5f, e), indicate the presence of channels through the garnet porphyroblasts, where fluids interacted to dissolve the original garnet and precipitate their dissolved load. (iii) The simultaneous formation of static euhedral glaucophane Amp_2 in the rock matrix (Fig. 7b, c), and occasionally alongside Cpx_4 and Grt_{2S} within atoll garnet porphyroblasts (Fig. 5f), further suggests the presence of an aqueous fluid phase during the atoll garnet formation. Mesostructural, microstructural, and mineral-chemical evidence suggest an internal origin for this fluid. (i) The studied eclogite-boudin is embedded within similar metabasites retrogressed to glaucophane-rich schists. (ii) Evidence of external fluid infiltration is minimal, limited to a late, thin albite + titanite + green amphibole vein (i.e., greenschist-facies assemblage) that cuts through the sample. Only locally, thin green amphiboles rim Amp_1, reflecting the chemical impact of this event. (iii) The nearly identical compositions of syn-Dp Amp_1 and post-Dp Amp_2 (Fig. 4c), along with the absence of significant mineral-chemical changes in rock-forming minerals, suggest that the composition of this fluid was not significantly different from that of the fluid already in equilibrium with the eclogite at peak conditions. For example, if the infiltrating fluid would have been sourced from the surrounding ultramafics or metasediments, we would expect an increase in Mg ± Si, or Si, Al, ± K, respectively, in the main minerals and/or the post-kinematic appearance of new minerals characterized by such elements. Taken together, this evidence supports the conclusion that the studied eclogitic boudin remained a closed system during exhumation to at least greenschist-facies conditions and that the fluid involved in the atoll garnet formation was internally derived.

To test whether a fluid internally derived during exhumation could explain the observed petrographic and mineral-chemical features, we performed additional calculations to assess the fluid composition expected to promote atoll garnet formation. It is well known that at H*P* conditions, H_2O increases its solvent capability, resulting in complex fluid compositions characterized by having all rock-forming elements variably dissolved within the fluid (e.g., Maffeis et al., 2021; Sverjensky et al., 2014). Following Manzotti et al. (2020), we fixed the amount of water in the unfractionated EBC I to that present in the system after the lawsonite breakdown at the metamorphic peak, because this was the last major dehydration reaction crossed by the sample (see above). As mentioned before, this choice is justified by the fact that Grt_1 was pervasively fractured before the growth of Grt_{2S} and Grt_{2N}; this process exposed the Grt_1 core and mantle to the matrix, re-opening the system and making them again available to participate in metamorphic reactions. With this bulk composition (see Table 1), we calculated the solute-bearing fluid composition in equilibrium with the peak and early decompression mineral assemblages using the lagged-speciation algorithm implemented in Perple_X (Connolly and Galvez, 2018; Galvez et al., 2015). The calculation results are reported in Fig. 13. The modelled fluid volume remains roughly constant at ~1.4 vol% along the heating and decompression *P*–*T* path connecting the peak Dp stage to the exhumation post-Dp stage (Fig. 13a). This value is in line with the porosity observed both in natural H*P* eclogites and in H*P* experiments (Angiboust and Raimondo, 2022 and references therein) and is representative of the amount of fluid that can be preserved interstitially in a rock system without being expelled. The modelled fluid is a rather dilute aqueous fluid having between 0.8 and 1.3 mol% of total dissolved load. Notably, the dissolved load, and thus the fluid solvent capability, increases during rock exhumation (Fig. 13b). The solute load is dominated by dissolved Si and Na (constituting 94 to 98 % of the dissolved load), with total dissolved SiO_2 ranging between ~0.8 and ~ 1 mol% (from 84 to 80 % of the dissolved load; Fig. 13c) and the total dissolved Na_2O ranges between 0.14 and 0.19 mol% (roughly 15 % of the dissolved load; Fig. 13d). Therefore, we suggest that the atoll garnet formation was a micro-scale mass-transfer process in which the Si-Na-aqueous fluid, upon infiltration through cracks, selectively dissolved the garnet core (Grt_{1C}) which was in larger disequilibrium with the fluid than any other garnet shell. Since the predicted solubility of Fe, Ca, Mg and Mn at 600–630 °C and 1.4–1.5 GPa is low, a Ca-poor garnet (Grt_{2S}) reprecipitated together with omphacitic Cpx_4, thanks to the nutrients given by the concomitantly dissolved Grt_{1C} and by the external (relative to the garnet core) Si and Na. As such, the following schematic type reaction can be envisioned for the atoll garnet formation (accounting also for the local Amp_2 found inside atoll garnet crystals):

$$Grt_{1C} + Fluid_{H_2O_{Si,Na}} = Grt_{2S} + Cpx_4 \pm Amp_2$$

Furthermore, chemical profiles across garnet show a slight increase in Mn concentration from the crystal boundary toward the inner part of the garnet rim. Such a feature might be explained by the predicted low solubility of Mn within aqueous fluids (here modelled to be around 10^{-8} to 10^{-9} mol% at 600–630 °C and 1.3–1.5 GPa). Such solubility might have been sufficient to allow for Mn diffusion through the interstitial fluid back into the Mn-poor Grt_{1R}, for which the Mn partition coefficient is expected to be much higher than for an aqueous fluid. At the same time, outside the atoll garnet, the same fluid is expected to rehydrate the rock matrix by reacting with the syn-Dp Cpx_3 to give the post-Dp Amp_2:

$$Cpx_3 + Fluid_{H_2O_{Si,Na}} = Amp_2$$

Overall, these processes consume the pore fluids (see fluid saturation surfaces right outside of the modelled *P*–*T* field for the post-Dp stage;

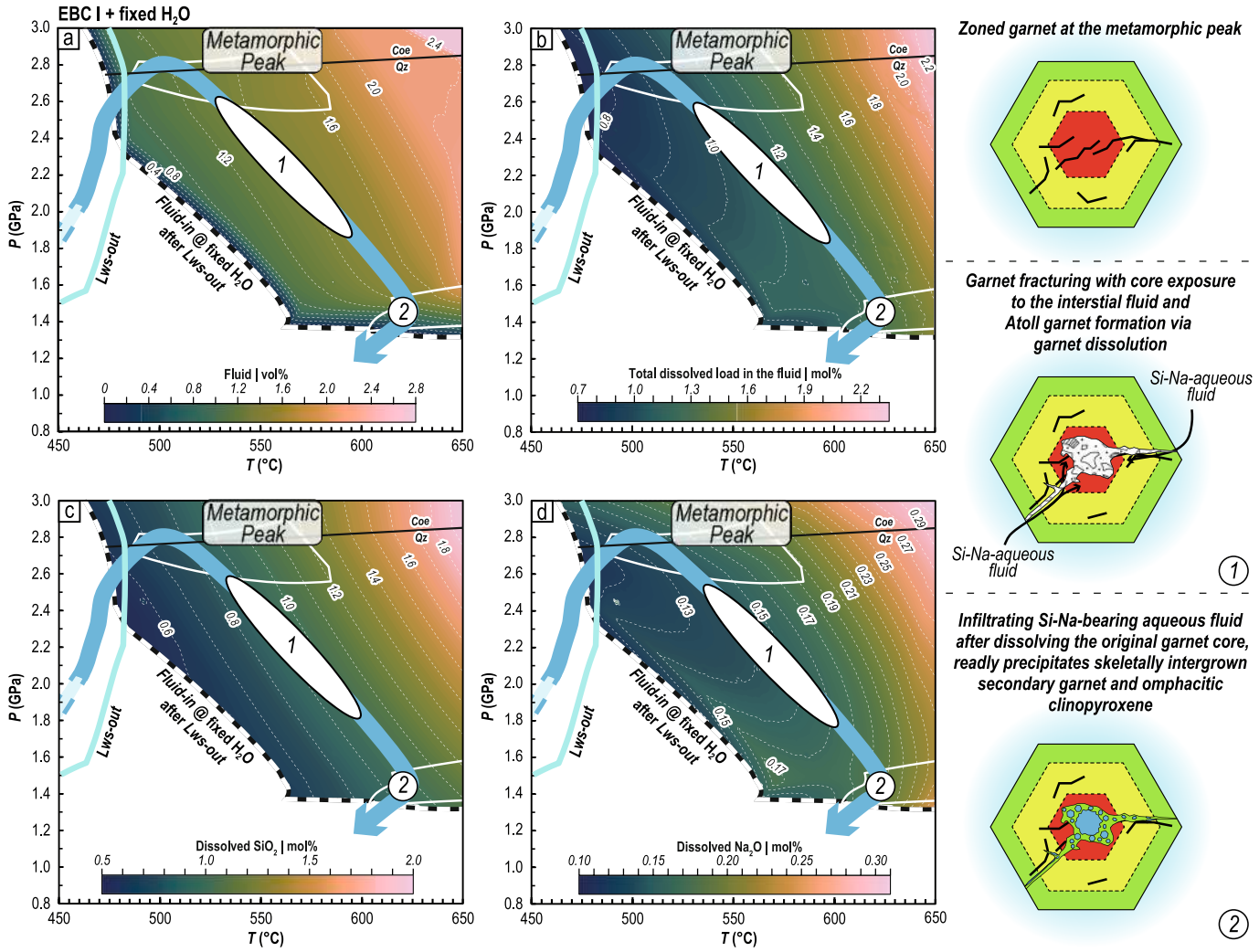

Fig. 13. Modelled solute-bearing fluid volume (a) and composition (b-d) in equilibrium with the studied eclogite during the peak to early decompression stages, and schematic sketch showing the fluid-mediated atoll garnet formation process.

Fig. 13) and effectively stop any further significant rock re-equilibration during exhumation.

5.3.2. *Garnet fracturing*

While the modelling presented above can explain the atoll garnet formation through fluid-mediated garnet dissolution and re-precipitation, the mechanism of garnet fracturing which allowed the interaction between garnet core and the pore fluid, remains to be discussed. Evidence of brittle deformation at the *P*-peak in the LPL has been described by Angiboust et al. (2011) and Locatelli et al. (2018) in the Monviso area, with the onset of brecciation at eclogite facies conditions. Also, coeval brittle-ductile deformation was reported in many exhumed eclogites from the LPL (e.g., at $P < 1.8$ GPa, see Ghignone et al., 2024). Following these studies, we can speculate that fluid infiltration due to microcracks in garnet may be related to differences in the fluid pressure (differential pore fluid pressure) inside and outside the garnet grains. It is known that metamorphic dehydration reactions transiently increase pore fluid pressure and trigger brittle-ductile cyclicity. During H*P* metamorphism and exhumation in subduction zones, significant volume changes within garnet porphyroblasts can occur due to the polymorphic transformation of minerals (e.g., coesite to quartz) or to dehydration reactions of included hydrous minerals (e.g., lawsonite breakdown), resulting in the development of microfractures (e.g., Bernaudin and Gueydan, 2018). In this case study, the inner garnet mantle is populated by paragonite+epidote polymineralic inclusions interpreted as pseudomorphs after former lawsonite (Fig. 7a; Supplementary Fig. 5b, c). Since lawsonite breakdown is a major dehydration reaction, we suggest that garnet fracturing might have been triggered by fluid released through this process during exhumation (Okazaki and Hirth, 2016). To test this hypothesis, we have performed further modelling of a representative inclusion-host system composed of minerals now forming the pseudomorphs after lawsonite (paragonite + epidote) and results are shown in Fig. 14a (see Methods for further details on the modelling strategy). This modelling shows that the lawsonite (Lws_{INC}) included in garnet (Grt_{HOST}) is involved in two major dehydration pulses along the inferred *P*–*T* path (Fig. 14b). The first one occurred soon after the metamorphic peak (~550 °C, ~2.4 GPa; Fig. 14) and the second one occurred halfway between the metamorphic peak and the post-Dp stage (~575 °C, ~2.1 GPa; Fig. 14). Notably, the Lws-out reaction modelled using the Grt + Lws local bulk composition is predicted to occur at a much higher temperature (ΔT ~ 70–100 °C) than in the surrounding rock, where it is predicted at anomalously low temperatures (i.e., ~480 °C, ~2.4 GPa, Figs. 10 and 11) compared to the results of experiments and modelling in typical mafic systems. The compositional difference between the Grt + Lws sub-system and the whole rock system is the key reason explaining the delayed breakdown of lawsonite included in garnet during retrograde metamorphism. The volume of the free fluid phase produced through these two stages of lawsonite breakdown increases from 2 vol% to 10 vol% and 13 vol%, respectively (Fig. 14c). Moreover, the overall volume change of the lawsonite sites

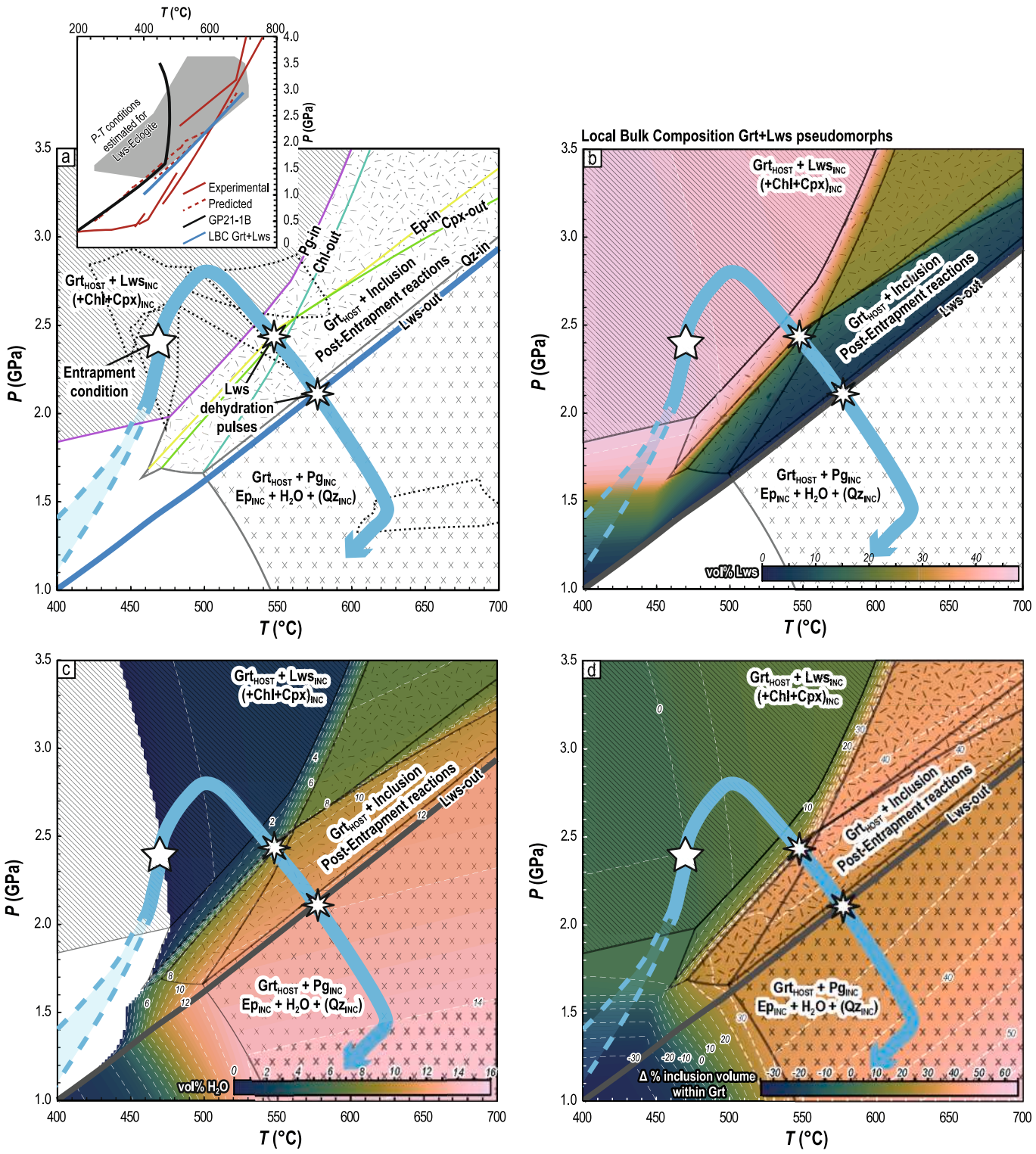

Fig. 14. Isochemical phase diagram modelled for a Grt_{HOST} + Lws_{INC} system depicting the post-entrapment reactions resulting in the Lws pseudomorphic replacement by epidote and paragonite. The Na necessary for paragonite might be potentially given by an included Na-rich Cpx (as is modelled here) or glaucophane. The whole rock isochemical phase diagram (Fig. 9, 10b) predicts the presence of a Na-rich Cpx (with $XNa > 0.77$) at blueschist-facies conditions along the inferred early pre-Dp stage. a) Simplified phase relations, where three macro phase fields are highlighted. The field on the left represents the initial stability field of host garnet + its mineral inclusions (Lws ± Chl, Cpx). The field in the middle represents the conditions at which the post-entrapment reactions between inclusions and the host garnet occur. The field on the right represents the currently observed assemblage with the paragonite and epidote inclusions within the garnet host. In the three fields of interest along the inferred *P–T* path, the volume of Chl + Cpx + Qz ranges from 18 vol% to 0.3 vol%, that of Grt ranges from 35 to 45 vol%, while those at of Ep and Pg are up to 27 and 18 vol%, respectively. The inset comparing Lws-out reaction topology is modified from Tsujimori and Ernst (2014) and references therein. b, c) Volume changes of Lws inclusions and amount of fluid produced through lawsonite breakdown. d) Change in the volume % of all the phases of the system excluding garnet.

within garnet is modelled to increase substantially by ~40 % at the first dehydration pulse (Fig. 14d). Occurring simultaneously in multiple (possibly hundreds) sites within the garnet mantle, this micro-scale process might have been able to generate enough tensile stress to induce garnet fracturing. A similar mechanical change has also been modelled for pseudomorphs after unbounded lawsonite porphyroblasts in blueschist-facies rocks from Syros (Hamelin et al., 2018).

Cyclic coeval continuous and discontinuous deformation occurring at H*P* conditions due to fluid pore pressure fluctuation may produce contemporaneous cyclic brittle and ductile deformation and potentially represent structures of paleo-seismicity, as episodic tremors and slow slip events (ETS; summary in Platt et al., 2024). Following previous results, we may speculate that slow slip was accommodated preferentially by slip on weaker layers or the main foliation, whereas contemporaneously episodic pulses of aqueous fluids produced by the destabilisation of hydrous minerals (like lawsonite) were responsible for garnet fracturing during high pore-fluid pressure. Garnet was already used as a metamorphic record of multiple seismic cycles during subduction processes (e.g., Angiboust et al., 2024 and references therein). Its rhythmic major element zoning is interpreted to be developed in response to growth-dissolution cycles driven by pressure pulses (Viete et al., 2018). Further studies are required to fully understand the potential link between atoll garnet formation and deep paleo-seismicity.

6. Conclusions

This study presents data from a coesite-glaucophane-bearing eclogite recording five different metamorphic stages, from before or at the onset of subduction, to the metamorphic peak and back during exhumation. Combining microstructural, minero-chemical and thermobarometric data, we highlight:

- A low-temperature stage (from prehnite-pumpellyite to greenschist-facies conditions; pre-H*P*) at <400 °C and < 0.6 GPa, recorded by mineral inclusions preserved within the core of some pyrite grains found within the core of garnet porphyroblasts, probably indicative of a pre-subduction metamorphic stage within the Alpine Tethys lower oceanic crust.
- An early prograde stage (early pre-Dp) at 450–480 °C, 1.9–2.6 GPa, recorded by the growth of garnet cores.
- A late prograde stage (late pre-Dp) at 420–510 °C, 2.3–2.9 GPa, recorded by the growth of garnet mantle and by its mineral inclusion pattern consisting of lawsonite in the inner mantle and omphacite in the outer mantle, testifying the transition from blueschist- to eclogite-facies conditions.
- The peak pressure stage (syn-Dp) at 480–580 °C, 2.75–2.9 GPa, recorded by the growth of garnet rims including coesite and by the development of glaucophane and omphacite along the main schistosity.
- An exhumation stage (post-Dp) at 600–630 °C, 1.3–1.5 GPa recorded by skeletally intergrown secondary garnet and omphacitic clinopyroxene developed within atoll garnet porphyroblasts and by euhedral post-kinematic glaucophane.

Compared with the *P–T* estimates from the literature for the LPL, our new data further corroborates the hypothesis that subduction of the oceanic lithosphere occurred with a relatively coherent evolution in the whole Western Alps, with a homogenous metamorphic H*P*-UH*P* peak at 500–580 °C, 2.5–2.8 GPa (Herviou et al., 2022). Our finding of coesite in this sector of the Western Alps fills the gap in the UH*P* metamorphic record of the LPL.

Moreover, we demonstrate that the characteristic atoll garnet microstructure records a fluid-mediated garnet fracturing-dissolution-reprecipitation event that occurred during rock exhumation at eclogite-facies conditions. Electrolytic fluid modelling allowed us to gain new insight into atoll garnet formation processes and to propose that a dilute aqueous fluid, with Si and Na as major dissolved rock-forming elements, was involved in the dissolution of old, fractured garnet cores and their replacement by an intergrowth of secondary garnet and omphacite.

Funding

This work has been partially financially supported by the Italian Ministry for Universities and Research (MUR) through the Ph.D. funds of A.M. The results presented here have been partially funded in the frame of the MIUR project “Dipartimenti di Eccellenza 2017 – Le Geoscienze per la società: risorse e loro evoluzione (work package 3, tasks 3.3 and 3.4)”. The work was partly supported by the Italian Ministry for Universities and Research (MUR) through the project “Dipartimenti di Eccellenza 2023-27”.

CRediT authorship contribution statement

A. Maffeis: Writing – review & editing, Writing – original draft, Visualization, Resources, Project administration, Methodology, Investigation, Funding acquisition, Data curation, Conceptualization. **A. Petroccia:** Writing – review & editing, Writing – original draft, Visualization, Resources, Project administration, Methodology, Investigation, Conceptualization. **S. Nerone:** Writing – review & editing, Writing – original draft, Visualization, Resources, Methodology, Investigation, Data curation. **F. Caso:** Writing – review & editing, Writing – original draft, Visualization, Methodology, Investigation, Funding acquisition. **A. Corno:** Writing – review & editing, Writing – original draft, Visualization, Methodology, Investigation, Data curation. **M. Bonazzi:** Writing – review & editing, Investigation, Data curation. **F. Boero:** Writing – review & editing, Visualization, Investigation, Data curation. **S. Corvò:** Writing – review & editing, Investigation, Data curation. **S. Ghignone:** Writing – review & editing, Investigation, Data curation. **C. Groppo:** Writing – review & editing, Validation, Supervision.

Declaration of competing interest

The authors declare that they have no known competing financial interests or personal relationships that could have appeared to influence the work reported in this paper.

Data Availability

All the data necessary to evaluate and replicate the presented calculations and conclusions can be found within the main text and the Supplementary Material.

Acknowledgements

Andrea Risplendente is thanked for EPMA analyses and maps. Mattia Gilio is thanked for the support during Raman analyses. Pierre Lanari and Jacob Forshaw are thanked for their insightful discussions and EPMA analyses. Nadia Malaspina is thanked for the editorial handling. Clement Herviou and an anonymous reviewer are thanked for their suggestions which have considerably increased the quality of the manuscript.

Appendix A. Supplementary data

Supplementary data to this article can be found online at https://doi.org/10.1016/j.lithos.2025.107981.

References

van Actherbergh, E., 2001. Data reduction software for LA-ICP-MS. Laser Ablation-ICP-Mass Spectrometry Earth Sci. Principles Appl. 239–243.

Agard, P., 2021. Subduction of oceanic lithosphere in the Alps: Selective and archetypal from (slow-spreading) oceans. Earth Sci. Rev. 103517. https://doi.org/10.1016/j.earscirev.2021.103517.

Agard, P., Handy, M.R., 2021. Ocean subduction dynamics in the Alps. Elements: Int. Magazine Mineral. Geochem. Petrol. 17 (1), 9–16. https://doi.org/10.2138/gselements.17.1.9.

Angiboust, S., Raimondo, T., 2022. Permeability of subducted oceanic crust revealed by eclogite-facies vugs. Geology 50 (8), 964–968. https://doi.org/10.1130/G50066.1.

Angiboust, S., Agard,, P., 2010. Initial water budget: the key to detaching large volumes of eclogitized oceanic crust along the subduction channel? Lithos 120, 453–474. https://doi.org/10.1016/j.lithos.2010.09.007.

Angiboust, S., Agard, P., Raimbourg, H., Yamato, P., Huet, B., 2011. Subduction interface processes recorded by eclogite-facies shear zones (Monviso, W. Alps). Lithos 127 (1–2), 222–238. https://doi.org/10.1016/j.lithos.2011.09.004.

Angiboust, S., Ioannidi, P.I., Muldashev, I., 2024. Garnet fracturing reveals ancient unstable slip events hosted in plate interface metasediments. Earth Planet. Sci. Lett. 640, 118794. https://doi.org/10.1016/j.epsl.2024.118794.

Assanelli, M., Roda, M., 2023. Multiscale structural study of metaophiolite of Val d'Ala, Northern slope (Piemonte Zone-Western Alps-Italy). Ofioliti 48 (2), 121–136. https://doi.org/10.4454/ofioliti.v48i2.565.

Bearth, P., 1967. Die Ophiolithe der Zone von Zermatt-Saas Fee. Beiträge zur Geologischen Karte der Schweiz, Neue Folge, p. 130.

Bernaudin, M., Gueydan, F., 2018. Episodic tremor and slip explained by fluid-enhanced microfracturing and sealing. Geophys. Res. Lett. 45 (8), 3471–3480. https://doi.org/10.1029/2018GL077586.

Bigi, G., Castellarin, A., Coli, M., Dal Piaz, G.V., Sartori, R., Scandone, P., Vai, G.B., 1990. Structural Model of Italy, Sheets 1–2: CNR. Progetto Fin, Geodinamica, SELCA Firenze.

Bovay, T., Rubatto, D., Lanari, P., 2021. Pervasive fluid-rock interaction in subducted oceanic crust revealed by oxygen isotope zoning in garnet. Contrib. Mineral. Petrol. 176 (7), 55. https://doi.org/10.1007/s00410-021-01806-4.

Bovay, T., Lanari, P., Rubatto, D., Smit, M., Piccoli, F., 2022. Pressure–temperature–time evolution of subducted crust revealed by complex garnet zoning (Theodul Glacier Unit, Switzerland). J. Metam. Geol. 40 (2), 175–206. https://doi.org/10.1111/jmg.12623.

Boyer, H., Smith, D.C., Chopin, C., Lasnier, B., 1985. Raman microprobe (RMP) determinations of natural and synthetic coesite. Physics and Chemistry of Minerals 12 (1), 45–48.

Brown, M., 2023. Some thoughts about eclogites and related rocks. Eur. J. Mineral. 35 (4), 523–547. https://doi.org/10.5194/ejm-35-523-2023.

Bullock, E.S., von der Handt, A., Halfpenny, A., 2025. Scanning electron microscopy, electron probe microanalysis, and electron backscatter diffraction in the geological sciences. Treatise Geochem. 3rd Ed., 8, 789–828.

Cao, D., Cheng, H., Zhang, L., Wang, K., 2018. Origin of atoll garnets in ultra-high-pressure eclogites and implications for infiltration of external fluids. J. Asian Earth Sci. 160, 224–238. https://doi.org/10.1016/j.jseaes.2018.04.030.

Carvalho, B.B., Bartoli, O., Cesare, B., Tacchetto, T., Gianola, O., Ferri, F., Aradi, L., Szabó, C., 2020. Primary CO2-bearing fluid inclusions in granulitic garnet usually do not survive. Earth Planet. Sci. Lett. 536, 116170. https://doi.org/10.1016/j.epsl.2020.116170.

Caso, F., Nerone, S., Petroccia, A., Bonasera, M., 2021. Geology of the southern Gran Paradiso Massif and lower Piedmont Zone contact area (middle Ala Valley, Western Alps, Italy). J. Maps 17 (2), 237–246. https://doi.org/10.1080/17445647.2021.1911869.

Caso, F., Petroccia, A., Nerone, S., Maffeis, A., Corno, A., Zucali, M., 2024. Comparison between 2D and 3D microstructures and implications for metamorphic constraints using a chloritoid-garnet-bearing mica schist. Eur. J. Mineral. 36 (3), 381–395. https://doi.org/10.5194/ejm-36-381-2024.

Chapman, T., Clarke, G.L., Piazolo, S., Daczko, N.R., 2019. Inefficient high-temperature metamorphism in orthogneiss. Am. Mineral. J. Earth Planet. Mater. 104 (1), 17–30. https://doi.org/10.2138/am-2019-6503.

Connolly, J.A., Galvez, M.E., 2018. Electrolytic fluid speciation by Gibbs energy minimization and implications for subduction zone mass transfer. Earth Planet. Sci. Lett. 501, 90–102. https://doi.org/10.1016/j.epsl.2018.08.024.

Connolly, J.A.D., 2009. The geodynamic equation of state: what and how. Geochem. Geophys. Geosyst. 10 (10), 1–19. https://doi.org/10.1029/2009GC002540.

Corno, A., Groppo, C., Borghi, A., Mosca, P., Gattiglio, M., 2023. To be or not to be Alpine: New petrological constraints on the metamorphism of the Chenaillet Ophiolite (Western Alps). J. Metam. Geol. 41 (6), 745–765. https://doi.org/10.1111/jmg.12716.

De Togni, M., Gattiglio, M., Ghignone, S., Festa, A., 2021. Pre-Alpine Tectono-Stratigraphic Reconstruction of the Jurassic Tethys in the High-pressure Internal Piedmont Zone (Stura di Viù Valley, Western Alps). Minerals 11 (4), 361. https://doi.org/10.3390/min11040361.

De Togni, M., Balestro, G., Rubatto, D., Castelli, D., Gattiglio, M., Festa, A., 2024. Late Jurassic magmatism in the Ligurian-Piedmont Ocean constrained by zircon ages of mafic and felsic meta-intrusives. Terra Nova 00, 1–11. https://doi.org/10.1111/ter.12723.

Evans, K.A., Powell, R., Holland, T.J.B., 2010. Internally consistent data for Sulphur-bearing phases and application to the construction of pseudosections for mafic greenschist facies rocks in Na2O–CaO–K2O–FeO–MgO–Al2O3–SiO2–CO2–O–S–H2O. J. Metam. Geol. 28 (6), 667–687. https://doi.org/10.1111/j.1525-1314.2010.00890.x.

Faryad, S.W., Klápová, H., Nosál, L., 2010. Mechanism of formation of atoll garnet during high-pressure metamorphism. Mineral. Mag. 74 (1), 111–126. https://doi.org/10.1180/minmag.2010.074.1.111.

Frezzotti, M.L., Selverstone, J., Sharp, Z.D., Compagnoni, R., 2011. Carbonate dissolution during subduction revealed by diamond-bearing rocks from the Alps. Nat. Geosci. 4 (10), 703–706. https://doi.org/10.1038/ngeo1246.

Fuhrman, M.L., Lindsley, D.H., 1988. Ternary-feldspar modeling and thermometry. Am. Mineral. 73 (3–4), 201–215.

Galliano, Y., Carbone, C., Balestra, V., Belmonte, D., De Waele, J., 2022. Secondary minerals from minothem environments in Fragnè Mine (Turin, Italy): preliminary results. Minerals 12 (8), 966. https://doi.org/10.3390/min12080966.

Galvez, M.E., Manning, C.E., Connolly, J.A., Rumble, D., 2015. The solubility of rocks in metamorphic fluids: a model for rock-dominated conditions to upper mantle pressure and temperature. Earth Planet. Sci. Lett. 430, 486–498. https://doi.org/10.1016/j.epsl.2015.06.019.

Gasco, I., Gattiglio, M., 2011. Geological map of the middle Orco Valley, Western Italian Alps. J. Maps 7 (1), 463–477. https://doi.org/10.4113/jom.2010.1121.

Ghignone, S., Balestro, G., Gattiglio, M., Borghi, A., 2020. Structural evolution along the Susa Shear Zone: the role of a first-order shear zone in the exhumation of meta-ophiolite units (Western Alps). Swiss J. Geosci. 113 (1), 17. https://doi.org/10.1186/s00015-020-00370-6.

Ghignone, S., Scaramuzzo, E., Bruno, M., Livio, F.A., 2023. A new UHP unit in the Western Alps: first occurrence of coesite from the Monviso Massif (Italy). Am. Mineral. 108 (7), 1368–1375. https://doi.org/10.2138/am-2022-8621.

Ghignone, S., Gilio, M., Borghini, A., Boero, F., Bruno, M., Scaramuzzo, E., 2024. Mineralogical and petrological constraints and tectonic implications of a new coesite-bearing unit from the Alpine Tethys oceanic slab (Susa Valley, Western Alps). Lithos 472, 107575. https://doi.org/10.1016/j.lithos.2024.107575.

Giuntoli, F., Menegon, L., Warren, C.J., 2018. Replacement reactions and deformation by dissolution and precipitation processes in amphibolites. J. Metam. Geol. 36 (9), 1263–1286. https://doi.org/10.1111/jmg.12445.

Godet, A., Raimondo, T., Guilmette, C., 2022. Atoll garnet: insights from LA-ICP-MS trace element mapping. Contrib. Mineral. Petrol. 177 (6), 57. https://doi.org/10.1007/s00410-022-01924-7.

Green, E., Holland, T., Powell, R., 2007. An order-disorder model for omphacitic pyroxenes in the system jadeite-diopside-hedenbergite-acmite, with applications to eclogitic rocks. Am. Mineral. 92 (7), 1181–1189. https://doi.org/10.2138/am.2007.2401.

Green, E.C.R., White, R.W., Diener, J.F.A., Powell, R., Holland, T.J.B., Palin, R.M., 2016. Activity–composition relations for the calculation of partial melting equilibria in metabasic rocks. J. Metam. Geol. 34 (9), 845–869. https://doi.org/10.1111/jmg.12211.

Groppo, C., Castelli, D., 2010. Prograde P–T evolution of a lawsonite eclogite from the Monviso meta-ophiolite (Western Alps): Dehydration and redox reactions during subduction of oceanic FeTi-oxide gabbro. J. Petrol. 51, 2489–2514. https://doi.org/10.1093/petrology/egq065.

Groppo, C., Beltrando, M., Compagnoni, R., 2009. P-T path of the UHP Lago di Cignana and adjoining HP meta-ophiolitic units: insights into the evolution of subducting tethyan slab. J. Metam. Geol. 27, 207–231. https://doi.org/10.1111/j.1525-1314.2009.00814.x.

Hamelin, C., Brady, J.B., Cheney, J.T., Schumacjer, J.C., Able, L.M., Sperry, A.J., 2018. Pseudomorphs after lawsonite from Syros, Greece. J. Petrol. 59, 2253–2384. https://doi.org/10.1093/petrology/egy099.

Hartmeier, P., Lanari, P., Forshaw, J.B., Markmann, T.A., 2024. Tracking garnet dissolution kinetics in 3D using deep learning grain shape classification. J. Petrol. 65 (3), egae005. https://doi.org/10.1093/petrology/egae005.

Hawthorne, F.C., Oberti, R., Harlow, G.E., Maresch, W.V., Martin, R.F., Schumacher, J. C., Welch, M.D., 2012. Nomenclature of the amphibole supergroup. Am. Mineral. 97 (11−12), 2031–2204. https://doi.org/10.2138/am.2012.4276.

Hernández-Uribe, D., Holder, R.M., Hernández-Montenegro, J.D., 2024. Eclogite thermobarometry: the consistency between conventional thermobarometry and forward phase-equilibrium modelling. J. Metam. Geol. 42 (1), 89–108. https://doi.org/10.1111/jmg.12747.

Herviou, C., Agard, P., Plunder, A., Mendes, K., Verlaguet, A., Deldicque, D., Cubas, N., 2022. Subducted fragments of the Liguro-Piemont Ocean, Western Alps: Spatial correlations and offscraping mechanisms during subduction. Tectonophysics 827, 229267. https://doi.org/10.1016/j.tecto.2022.229267.

Herviou, C., Bonnet, G., Angiboust, S., Cambeses, A., Raimondo, T., 2025. Petrochronology of high-pressure veins reveals the evolution of fluid sources in subducted oceanic crust (Rocciavrè Eclogites, W. Alps). J. Metam. Geol. 0, 1–32. https://doi.org/10.1111/jmg.12806.

Holland, T.J., Green, E.C., Powell, R., 2018. Melting of peridotites through to granites: a simple thermodynamic model in the system KNCFMASHTOCr. J. Petrol. 59 (5), 881–900. https://doi.org/10.1093/petrology/egy048.

Holland, T.J.B., Powell, R., 1998. An internally consistent thermodynamic dataset for phases of petrological interest. J. Metam. Geol. 16, 309–343. https://doi.org/10.1111/j.1525-1314.1998.00140.x.

Holland, T.J.B., Powell, R., 2011. An improved and extended internally consistent thermodynamic dataset for phases of petrological interest, involving a new equation of state for solids. J. Metam. Geol. 29, 333–383. https://doi.org/10.1111/j.1525-1314.2010.00923.x.

van Keken, P.E., Wilson, C.R., 2023. An introductory review of the thermal structure of subduction zones: III—Comparison between models and observations. Prog Earth Planet Sci 10 (1), 57. https://doi.org/10.1186/s40645-023-00573-z.

Kohn, M.J., 2020. A refined zirconium-in-rutile thermometer. Am. Mineral. 105 (6), 963–971. https://doi.org/10.2138/am-2020-7091.
Kulhánek, J., Faryad, S.W., 2023. Compositional changes in garnet: trace element transfer during eclogite-facies metamorphism. Contrib. Mineral. Petrol. 178 (10), 68. https://doi.org/10.1007/s00410-023-02050-8.
Kulhánek, J., Faryad, S.W., Jedlicka, R., Svojtka, M., 2021. Dissolution and reprecipitation of garnet during eclogite-facies metamorphism; major and trace element transfer during atoll garnet formation. J. Petrol. 62 (11), egab077. https://doi.org/10.1093/petrology/egab077.
Lanari, P., Vidal, O., De Andrade, V., Dubacq, B., Lewin, E., Grosch, E.G., Schwartz, S., 2014. XMapTools: a MATLAB©-based program for electron microprobe X-ray image processing and geothermobarometry. Comput. Geosci. 62, 227–240. https://doi.org/10.1016/j.cageo.2013.08.010.
Leake, B.E., Woolley, A.R., Arps, C., Birch, W.D., Gilbert, M.C., Grice, J.D., Hawthorne, F. C., Kato, A., Kisch, H.J., Krivovichev, V.G., Linthout, K., Laird, J., Mandarino, J.A., Maresch, W.V., Nickel, E.H., Rock, N.M.S., Schumacher, J.C., Smith, D.C., Stephenson, N.C.N., Ungaretti, L., Whittaker, E.J.W., Youzhi, G., 1997. Nomenclature of amphiboles. Am. Mineral. 82, 1019–1037. https://doi.org/10.1180/minmag.1997.061.405.13.
Leardi, L., Rossetti, P., 1985. Caratteri geologici e petrografici delle metaofioliti della Val d'Ala (Valli di Lanzo, Alpi Graie). Bollettino Dell'associazione Mineraria Subalpina 22, 422–441.
Locatelli, M., Verlaguet, A., Agard, P., Federico, L., Angiboust, S., 2018. Intermediate-depth brecciation along the subduction plate interface (Monviso eclogite, W. Alps). Lithos 320, 378–402. https://doi.org/10.1016/j.lithos.2018.09.028.
Locock, A.J., 2014. An Excel spreadsheet to classify chemical analyses of amphiboles following the IMA 2012 recommendations. Comput. Geosci. 62, 1–11. https://doi.org/10.1016/j.cageo.2013.09.011.
Luoni, P., Rebay, G., Spalla, M.I., Zanoni, D., 2018. UHP Ti-chondrodite in the Zermatt-Saas serpentinite: Constraints on a new tectonic scenario. Am. Mineral. 103 (6), 1002–1005. https://doi.org/10.2138/am-2018-6460.
Maffeis, A., Ferrando, S., Connolly, J.A., Groppo, C., Frezzotti, M.L., Castelli, D., 2021. Thermodynamic analysis of HP-UHP fluid inclusions: the solute load and chemistry of metamorphic fluids. Geochim. Cosmochim. Acta 315, 207–229. https://doi.org/10.1016/j.gca.2021.08.044.
Maffeis, A., Frezzotti, M.L., Connolly, J.A.D., Castelli, D., Ferrando, S., 2024. Sulfur disproportionation in deep COHS slab fluids drives mantle wedge oxidation. Sci. Adv. 10 (12), eadj2770. https://doi.org/10.1126/sciadv.adj2770.
Manzotti, P., Ballèvre, M., Pitra, P., Putlitz, B., Robyr, M., Müntener, O., 2020. The growth of sodic amphibole at the greenschist-to blueschist-facies transition (Dent Blanche, Western Alps): bulk-rock chemical control and thermodynamic modelling. J. Petrol. 61 (4), egaa044. https://doi.org/10.1093/petrology/egaa044.
Manzotti, P., Schiavi, F., Nosenzo, F., Pitra, P., Ballèvre, M., 2022. A journey towards the forbidden zone: a new, cold, UHP unit in the Dora-Maira Massif (Western Alps). Contrib. Mineral. Petrol. 177 (6), 59. https://doi.org/10.1007/s00410-022-01923-8.
Manzotti, P., Regis, D., Petts, D.C., Graziani, R., Polivchuk, M., 2024. Formation of multistage garnet grains by fragmentation and overgrowth constrained by microchemical and microstructural mapping. J. Metam. Geol. 42 (4), 471–496. https://doi.org/10.1111/jmg.12761.
Morimoto, N., 1988. Nomenclature of pyroxenes. Am. Mineral. 7 (3), 1133–1198. https://doi.org/10.1007/BF01226262.
Nerone, S., Petroccia, A., Caso, F., Dana, D., Maffeis, A., 2024. Assessing the importance of H2O content in the tectono-metamorphic evolution of shear zones: a case study from the Dora-Maira Massif (Western Alps). J. Metam. Geol. 42 (2), 171–196. https://doi.org/10.1111/jmg.12750.
Okazaki, K., Hirth, G., 2016. Dehydration of lawsonite could directly trigger earthquakes in subducting oceanic crust. Nature 530 (7588), 81–84. https://doi.org/10.1038/nature16501.
Platt, J.P., Grujic, D., Phillips, N.J., Piazolo, S., Schmidt, D.A., 2024. Geological fingerprints of deep slow earthquakes: a review of field constraints and directions for future research. Geosphere 20 (4), 981–1004. https://doi.org/10.1130/GES02722.1.
Plunder, A., Agard, P., Dubacq, B., Chopin, C., Bellanger, M., 2012. How continuous and precise is the record of P–T paths? Insights from combined thermobarometry and thermodynamic modelling into subduction dynamics (Schistes Lustrés, W. Alps). J. Metam. Geol. 30 (3), 323–346. https://doi.org/10.1111/j.1525-1314.2011.00969.x.
Reinecke, T., 1998. Prograde high-to ultrahigh-pressure metamorphism and exhumation of oceanic sediments at Lago di Cignana, Zermatt-Saas Zone, western Alps. Lithos 42 (3–4), 147–189. https://doi.org/10.1016/S0024-4937(97)00041-8.
Rocholl, A.B., Simon, K., Jochum, K.P., Bruhn, F., Gehann, R., Kramar, U., Luecke, W., Molzahn, M., Pernicka, E., Seufert, M., Spettel, M., Stummeier, J., 1997. Chemical Characterisation of NIST Silicate Glass Certified Reference Material SRM 610 by ICP-MS, TIMS, LIMS, SSMS, INAA, AAS and PIXE. Geostandards Newsletter 21 (1), 101–114. https://doi.org/10.1111/j.1751-908X.1997.tb00537.x.
Rubatto, D., Hermann, J., 2001. Exhumation as fast as subduction? Geology 29 (1), 3–6. https://doi.org/10.1130/0091-7613(2001)029<0003:EAFAS>2.0.CO;2.
Sandrone, R., Leardi, L., Rossetti, P., Compagnoni, R., 1986. P-T conditions for the eclogitic re-equilibration of the metaophiolites from Val d'Ala di Lanzo (internal Piemontese zone, Western Alps). J. Metam. Geol. 4, 161–178. https://doi.org/10.1111/j.1525-1314.1986.tb00345.x.
Sverjensky, D.A., Stagno, V., Huang, F., 2014. Important role for organic carbon in subduction-zone fluids in the deep carbon cycle. Nat. Geosci. 7 (12), 909–913. https://doi.org/10.1038/ngeo2291.
Tsujimori, T., Ernst, W.G., 2014. Lawsonite blueschists and lawsonite eclogites as proxies for palaeo-subduction zone processes: a review. J. Metam. Geol. 32 (5), 437–454. https://doi.org/10.1111/jmg.12057.
Tsujimori, T., Liou, J.G., 2007. Significance of the Ca-Na pyroxene-lawsonite-chlorite assemblage in blueschist-facies metabasalts: an example from the renge metamorphic rocks, Southwest Japan. Int. Geol. Rev. 49, 416–430. https://doi.org/10.2747/0020-6814.49.5.416.
Ulmer, P., 1986. NORM - Program for Cation and Oxygen Mineral Norms. Computer Library, Institut für Mineralogie und Petrographie, ETH-Zentrum, ETH-Zentrum.
Viete, D.R., Hacker, B.R., Allen, M.B., Seward, G.G., Tobin, M.J., Kelley, C.S., Duckworth, A.R., 2018. Metamorphic records of multiple seismic cycles during subduction. Science advances 4 (3), eaaq0234.
Warr, L.N., 2021. IMA–CNMNC approved mineral symbols. Mineral. Magazine 85 (3), 291–320. https://doi.org/10.1180/mgm.2021.43.
White, R.W., Powell, R., Holland, T.J.B., Johnson, T.E., Green, E.C.R., 2014. New mineral activity–composition relations for thermodynamic calculations in metapelitic systems. J. Metam. Geol. 32 (3), 261–286. https://doi.org/10.1111/jmg.12071.